

1 **Title: Nucleolar stress controls mutant Huntingtin toxicity and monitors**

2 **Huntington's disease progression**

3 **Running title: Nucleolar homeostasis in HD**

4 Aynur Sönmez^{1,2}, Rasem Mustafa^{1,3}, Salome T. Ryll^{1,3}, Francesca Tuorto⁴, Ludivine
5 Wacheul², Donatella Ponti^{3,5}, Christian Litke³, Tanja Hering⁶, Kerstin Kojer⁶, Jenniver Koch¹,
6 Claudia Pitzer⁷, Joachim Kirsch³, Andreas Neueder⁶, Grzegorz Kreiner⁸, Denis L.J.
7 Lafontaine², Michael Orth^{6,#}, Birgit Liss^{1,9,#}, Rosanna Parlato^{1,3,10,#,*}

8

9 ¹ Institute of Applied Physiology, Ulm University, Ulm, Germany

10 ² RNA Molecular Biology, Fonds de la Recherche Scientifique (F.R.S./FNRS), Université
11 Libre de Bruxelles (ULB), Biopark campus, Gosselies, Belgium

12 ³ Institute of Anatomy and Cell Biology, Heidelberg University, Heidelberg, Germany

13 ⁴ Division of Biochemistry, Mannheim Institute for Innate Immunoscience (MI3), Medical
14 Faculty Mannheim, Heidelberg University, Mannheim and Center for Molecular Biology
15 of Heidelberg University (ZMBH), DKFZ-ZMBH Alliance, Heidelberg, Germany

16 ⁵ Department of Medical-Surgical Sciences and Biotechnologies, University of Rome
17 "Sapienza", Rome, Italy

18 ⁶ Department of Neurology, Ulm University, Ulm, Germany

19 ⁷ Interdisciplinary Neurobehavioral Core (INBC), Heidelberg University, Heidelberg, Germany

20 ⁸ Maj Institute of Pharmacology, Department of Brain Biochemistry, Polish Academy of
21 Sciences, Krakow, Poland

22 ⁹ Linacre & New College, University of Oxford, Oxford, UK

23 ¹⁰ Division of Neurodegenerative Disorders, Department of Neurology, Mannheim Center for
24 Translational Neuroscience, Medical Faculty Mannheim Heidelberg University, Mannheim,
25 Germany

26 # shared last author

27

- 1 *** Correspondence to:**
- 2 Dr. Rosanna Parlato
- 3 E-Mail: rosanna.parlato@medma.uni-heidelberg.de
- 4 Phone: +49 621 383 5611; Fax: +49 621 383 8459

1 **Abstract**

2 Transcriptional and cellular stress surveillance deficits are hallmarks of Huntington's disease
3 (HD), a fatal autosomal dominant neurodegenerative disorder, caused by a pathological
4 expansion of CAG repeats in the Huntingtin (*HTT*) gene. The nucleolus, a dynamic nuclear
5 biomolecular condensate and the site of ribosomal RNA (rRNA) transcription, is implicated in
6 the cellular stress response and in protein quality control. While the exact pathomechanisms
7 of HD remain unclear, the impact of nucleolar dysfunction on HD pathophysiology *in vivo* is
8 elusive. Here we identified aberrant maturation of rRNA and decreased translational rate in
9 association with human mutant Huntingtin (mHTT) expression. Genetic disruption of
10 nucleolar integrity in vulnerable striatal neurons of the R6/2 HD mouse model decreases
11 mHTT disperse state in the nucleus, exacerbating the motor deficits. The protein
12 nucleophosmin 1 (NPM1), important for nucleolar integrity and rRNA maturation, loses its
13 nucleolar localization. NPM1 de-localization occurs in the striatum and in the skeletal muscle
14 of the progressive zQ175 knock-in HD mouse model, mimicking the phenotype of HD
15 patients in skeletal muscle biopsies. Taken together, we showed that nucleolar integrity
16 regulates the formation of mHTT inclusions *in vivo*, and identified NPM1 as a novel, readily
17 detectable peripheral histopathological marker of HD progression.

18

19 **Keywords (5)**

20 Nucleolus; proteostasis; dopaminergic neuron; proteinopathy; nucleophosmin 1

1 **Abbreviations**

2 CNN: convolutional neural network, DAPI (4',6-diamidino-2-phenylindole), DBS: disease
3 burden score, D1R: dopamine receptor 1, D2R: dopamine receptor 2, DTT: Dithiothreitol,
4 ECL: Electrochemiluminescence, EDTA: Ethylenediaminetetraacetic acid, GAPDH:
5 Glyceraldehyde 3-phosphate dehydrogenase, HD: Huntington's disease; HPRT:
6 Hypoxanthine-guanine phosphoribosyltransferase, ISH: *in situ* hybridization, Metap1:
7 Methionine aminopeptidase 1, mRNA: messenger RNA, mHTT: mutant Huntingtin, NCL:
8 nucleolin, NPM1: nucleophosmin 1, NSS: normal swine serum, PBS: phosphate-buffered
9 saline, PFA: paraformaldehyde, PMSF: phenylmethylsulfonyl fluoride, PVDF: polyvinylidene
10 fluoride, pre-rRNA: precursor rRNA, qRT-PCR: quantitative real time PCR, rRNA: ribosomal
11 RNA, ROI: region of interest; STED: STimulated Emission Depletion, SUnSET: SURface
12 SEnsing of Translation, TBS: Tris-buffered saline, TFC: total functional capacity, TIF-IA:
13 transcription initiation factor IA, TMS: total motor score, UHDRS: united Huntington's disease
14 rating scale
15

1 **Introduction**

2 Dysregulation of rRNA biogenesis represents an emerging mechanism in several
3 progressive neurodegenerative diseases characterized by proteinopathy (Aladesuyi
4 Arogundade O *et al.*, 2019; Amer-Sarsour F and Ashkenazi A, 2019; Herrmann D and
5 Parlato R, 2018; Lee J *et al.*, 2014; Parlato R and Bierhoff H, 2015; Schludi MH *et al.*, 2015).
6 Ribosomal RNA synthesis in the nucleolus - the most prominent nuclear compartment and a
7 multilayered bio-molecular condensate - is tightly linked to the cell wellbeing, and it is highly
8 responsive to cellular stress (Boulon S *et al.*, 2010; Sharifi S and Bierhoff H, 2018). Nucleolar
9 stress is a p53-dependent anti-tumoral surveillance pathway activated upon ribosome
10 biogenesis dysfunction (Nicolas E *et al.*, 2016). The shape of the nucleolus, its size, and the
11 number of nucleoli per cell nucleus may change upon stress and in disease, reflecting
12 changes in its function (Lafontaine DLJ *et al.*, 2020). These properties have started to be
13 explored as disease biomarkers (Derenzini M *et al.*, 2009; Stamatopoulou V *et al.*, 2018).
14 Huntington' disease (HD) is caused by the expansion of CAG repeats in the exon 1 of the
15 huntingtin (*HTT*) gene (Group THsDCR, 1993). This autosomal dominant mutation results in
16 an abnormal polyglutamine expansion in the Huntingtin protein with toxic effects (Caron NS
17 *et al.*, 2018). Typical clinical hallmarks include motor, cognitive and psychiatric symptoms
18 (Ghosh R and Tabrizi SJ, 2018). Dopaminoceptive medium spiny neurons of the striatum, a
19 component of the basal ganglia, are particularly vulnerable to neurodegeneration, along with
20 reduced connectivity in regional and whole brain cortico-caudate networks that highly
21 correlate with cognitive and motor deficits (McColgan P *et al.*, 2015). Other non-neuronal
22 features include metabolic and immune problems, malfunction of skeletal muscle, and body
23 weight loss (Bates GP *et al.*, 2015; Dayalu P and Albin RL, 2015; Rodinova M *et al.*, 2019).
24 The length of the expanded CAG tract in the mutant *HTT* gene partially accounts for the
25 variability in the clinical HD onset (Consortium. GMoHsD, 2019; Ghosh R and Tabrizi SJ,
26 2018; Stuitje G *et al.*, 2017). Multiple pathophysiological mechanisms may contribute to HD
27 (Saudou F and Humbert S, 2016). Mutant HTT (mHTT) protein forms nuclear and
28 cytoplasmic inclusions that interfere with almost all aspects of cell physiology, from nuclear

1 transcription dysregulation to mitochondrial dysfunction, and compromised quality control
2 mechanisms, among many others (Francelle L *et al.*, 2017; Liot G *et al.*, 2017; McColgan P
3 and Tabrizi SJ, 2018; Rai SN *et al.*, 2019).

4 Previous studies showed that mHTT interferes with rDNA transcription and with the integrity
5 of the nucleolus (Hilditch-Maguire P *et al.*, 2000; Jesse S *et al.*, 2017; Kreiner G *et al.*, 2013;
6 Lee J *et al.*, 2011; Lee J *et al.*, 2014; Trettel F *et al.*, 2000; Tsoi H and Chan HY, 2013). In
7 the striatum of the R6/2 transgenic mice, the *de novo* transcription of rRNA is impaired
8 (Kreiner G *et al.*, 2013). Because of its rapid pathological progression (Mangiarini L *et al.*,
9 1996), this HD mouse model is commonly used for preclinical studies.

10 Several mechanisms have been proposed to explain how mHTT affects rRNA transcription
11 (Jesse S *et al.*, 2017; Lee J *et al.*, 2011; Tsoi H and Chan HY, 2013). mHTT protein acts on
12 the acetyltransferase CBP (CREB-binding protein), required for the activity of the RNA
13 polymerase I (Pol I) (Lee J *et al.*, 2011; Lee J *et al.*, 2014). Moreover, *mHTT* messenger
14 RNAs down-regulate rRNA transcription by interacting with the nucleolar protein nucleolin
15 (NCL), that plays multiple roles in rRNA synthesis, ribosome biogenesis and nucleolar
16 structure maintenance (Cong R *et al.*, 2012; Tsoi H and Chan HY, 2013; Tsoi H *et al.*, 2012).
17 PGC-1alpha (peroxisome proliferator-activated receptor gamma co-activator 1alpha), a
18 master regulator of mitochondrial biogenesis, which is transcriptionally repressed by mHTT,
19 also controls ribosomal DNA transcription in the nucleolus (Jesse S *et al.*, 2017). Importantly,
20 Brain Derived Neurotrophic Factor known to sustain striatal neuron survival and
21 downregulated in HD (Xie Y *et al.*, 2010; Zuccato C *et al.*, 2001), stimulates the activity of the
22 transcription initiation factor-1A (TIF-1A), essential for the recruitment of the RNA Pol I at the
23 ribosomal promoters (Gomes C *et al.*, 2011).

24 An interesting role of the nucleolus is its involvement in protein quality control to prevent the
25 irreversible aggregation of misfolded proteins, a mechanism often altered in several
26 aggregate-forming neurodegenerative diseases (Frottin F *et al.*, 2019; Nollen EA *et al.*,
27 2001). In particular, the nucleolar protein nucleophosmin-1 (NPM1) appears to have a

1 chaperone-like function in shielding the surfaces of potentially toxic aggregates (Woerner
2 AC, Frottin F Science 2016).

3 Despite the multiple relationships between transcriptional, metabolic and quality control
4 functions of the nucleolus and HD pathophysiological, the impact of nucleolar dysregulation
5 on HD progression *in vivo* has not been systematically addressed. It also remained
6 unexplored whether different disease stages are associated with context-specific changes in
7 nucleolar transcription and integrity. Ultimately, cytomorphological nucleolar alterations
8 related to HD pathophysiology in peripheral tissues might represent novel metabolic markers
9 to monitor disease progression and treatment response.

10 To gain insight into the mechanistic relationship between nucleolar dysfunction and disease
11 progression, we investigated the consequences of nucleolar stress on mHTT inclusions and
12 motor symptoms in R6/2 mice. We used a functional genomic approach to inhibit RNA Pol I
13 transcriptional activity in vulnerable striatal neurons of these mice. We have previously
14 shown that the conditional ablation of *Tif-1a* in medium spiny neurons of the striatum that
15 express the dopamine 1 receptor (D1R) mimics a condition of progressive nucleolar stress *in*
16 *vivo* (Kreiner G *et al.*, 2013). Given that TIF-1A is targeted by several kinase cascades and
17 integrates multiple signaling pathways, it represents an ideal molecular target to regulate
18 rDNA transcription in a cell-type specific fashion (Drygin D *et al.*, 2010; Parlato R and Kreiner
19 G, 2013). We found that rRNA processing deficits are associated with loss of NPM1
20 nucleolar localization in a relevant neuronal model expressing human mHTT, suggesting a
21 novel nucleolar stress-dependent pathophysiological mechanism. Finally, we reported similar
22 subcellular distribution of NPM1 in skeletal muscle of a gradually progressive mouse model
23 of HD, and in biopsies of HD patients at pre- and early symptomatic stages, establishing this
24 characteristic as a reliable disease read-out.

25

1 **Results**

2 **Expression of the human Huntingtin polyQ111 mutation alters nucleophosmin 1** 3 **localization, pre-rRNA processing and translation**

4 To investigate the functional impact of mHTT expression on ribosome biogenesis and
5 function, we analyzed a mouse cell model of Huntington's disease derived from embryonic
6 striatum and expressing a chimeric human-mouse mutant huntingtin (Trettel F *et al.*, 2000).
7 The StHdhQ111/Q111 cells (abbreviated "Q111/111") contain the polyQ111 mutation
8 encoded by the CAG expansion on both alleles in the Huntingtin gene. As control, we used
9 Q7/Q7 cells that express a non-pathological 7-glutamine wild-type protein on both alleles
10 **(Fig. 1)**. In this model, the localization of the scaffold protein nucleophosmin (NPM1) present
11 in the nucleolar granular component, where late steps of ribosomal subunit assembly occur,
12 was reduced (ca. 30%) in the Q111/111 cells in comparison with the control **(Fig. 1A, B)**.
13 Importantly, nucleolin (NCL), another nucleolar protein, did not show any significance
14 differences in abundance or distribution **(Fig. 1A, B)**.

15 To test if mHTT expression impacts pre-rRNA processing, total RNA was extracted from cells
16 expressing each construct, and separated on denaturing agarose gels. Mature rRNAs were
17 visualized by ethidium bromide staining **(Fig. 1F)** and quantified from electropherograms.
18 Precursor rRNAs were detected with specific radio-actively labelled probes **(Fig 1C-E)**.
19 We observed no gross alteration in the steady-state accumulation of the large mature rRNAs,
20 the 18S and 28S rRNAs **(Fig. 1F)**. The canonical pre-rRNA processing intermediates (29S,
21 34S, 43S, 45S, 46S, and 47S) detected with probe LD4098 also accumulated normally **(Fig.**
22 **1D)**. However, close inspection of the imaging plates reproducibly revealed additional low-
23 abundant pre-rRNA intermediates, referred to as '1', '2', '3', and '4' (in red in **Fig. 1D, E)**.
24 Note that species '2' and '3' appeared as a doublet, which was well-resolved on longer
25 migration **(Fig. 1E)**, for example lanes 17-19). Species '2', '3' and '4' visible in the reference
26 cells (Q7/7) corresponded to extended forms of the 34S pre-rRNA. Cells that expressed the
27 Q111/Q111 mutation, showed a novel band, labeled as '1' (lanes 11-16, highlighted in a red
28 box). Interestingly, when species '1' was detected, '2' was not, pointing to a precursor-

1 product relationship that was specific to the Q111/111 cells. Remarkably, the cryptic species
2 '1' was not observed in the heterozygous cells (Q7/Q111), indicating that sufficient amounts
3 of Q111/111 huntingtin must be expressed for processing to be altered.

4 We conclude that Q111/111 cells display qualitative differences in pre-rRNA processing, i.e.
5 alterations in RNA cleavage kinetics.

6 To investigate whether the processing alterations caused by mHTT expression impacts
7 translation, we performed polysomal analysis in the Q7/7 and Q111/111 cells
8 **(Supplementary Fig. 1A, B)**. Velocity gradient centrifugation allows to separate and to
9 quantify free ribosomal subunits (40S, 60S), monosomes (80S), and polysomes, and it is a
10 good proxy of global protein synthesis. Polysomal profiles revealed a deficit (ca. 20%,
11 $p=0.04$) in global translation, analyzed by the reduction of polysomal fraction in Q111/111
12 cells, while the number of ribosomal subunits was similar to that of Q7/7 cells
13 **(Supplementary Fig. 1A, B)**. This effect on translation was confirmed by use of the SURface
14 SEnsing of Translation (SUnSET) assay which monitors translation rates by labeling nascent
15 proteins with the amino-acid analog puromycin **(Supplementary Fig. 1C, D)**. A significant
16 reduction (ca. 30%, $p=0.009$) was observed in Q111/11 cells by comparison to control Q7/7
17 cells **(Supplementary Fig. 1C, D)**.

18 In summary, expression of mHTT in a cellular model of Huntington's disease was associated
19 with the specific loss of NPM1 nucleolar localization, the activation of cryptic pre-rRNA
20 processing, and reduced global translation.

21

22 **Nucleolar stress exacerbates mHTT neuropathology and motor behavior deficits in the** 23 **R6/2 model of Huntington's disease**

24 To investigate the impact of nucleolar stress on HD neuropathology, we genetically inhibited
25 nucleolar function in striatal medium spiny neurons of the R6/2 transgenic mouse model of
26 HD **(Fig. 2 and Supplementary Fig. 2)**. In particular, using the Cre-loxP system we
27 conditionally ablated the transcription factor TIF-IA, essential for the activity of the RNA
28 Polymerase I, in dopamine-receptive neurons of R6/2 mice, and we generated double mutant

1 R6/2; TIF-IA^{D1Cre} mice (abbreviated “dm”) (**Fig. 2**). We have previously shown that lack of
2 TIF-IA in striatal medium spiny neurons in the TIF-IA^{D1Cre} mice inhibited rRNA synthesis and
3 relocated nucleolar proteins to the nucleoplasm, mimicking a condition of nucleolar stress in
4 striatal neurons by 4 weeks of age (Kreiner G *et al.*, 2013).
5 Confocal microscopy on striatal sections immunolabeled by the nucleolar markers NPM1 and
6 NCL showed that in control mice at 9 weeks, the nucleolus was visible as a circular structure
7 within the nucleus (**Fig. 2A**). At the same age in the TIF-IA^{D1Cre} mice, the percentage of DAPI
8 labeled nuclei with NPM1 and NCL positive nucleoli was strongly decreased (ca. 90%) in
9 comparison to control littermates (**Supplementary Fig. 2A**). In the R6/2 mice, both NPM1
10 and NCL maintained a ring-like organization, however NPM1 signal was diffuse (**Fig. 2A and**
11 **Supplementary Fig. 2A**). In addition, NPM1 surrounded the cargo protein p62/SQSTM1
12 immunopositive nuclear aggregates in both the R6/2 and R6/2; TIF-IA^{D1Cre} mice (**Fig. 2A**).
13 Next, we compared the accumulation and distribution of mHTT in the R6/2 and in the R6/2;
14 TIF-IA^{D1Cre} mice, by immunofluorescence using the EM48 antibody. As expected, mHTT was
15 absent in striatal sections from control and TIF-IA^{D1Cre} mice (**Fig. 2A**). In the R6/2 and R6/2;
16 TIF-IA^{D1Cre} mice, mHTT was visible as intranuclear inclusions and scattered in the
17 nucleoplasm (**Fig. 2A**). The number and size of intra-nuclear inclusions containing mHTT
18 was comparable between R6/2 and the R6/2; TIF-IA^{D1Cre} littermates (**Supplementary Fig.**
19 **2B**). To gain further insight into the mHTT nuclear distribution upon induction of nucleolar
20 stress, we measured the ratio between the intensity of mHTT signal in the nucleoplasm and
21 in the nuclear inclusion bodies. Such ratio was about 30% lower in the R6/2; TIF-IA^{D1Cre} mice,
22 suggesting that nucleolar stress alters mHTT distribution and reduces its diffuse state (**Fig.**
23 **2B**). Disruption of nucleolar integrity determined by measuring nucleolin intensity in the DAPI
24 stained nucleus in the R6/2 and in the R6/2; TIF-IA^{D1Cre} mice, correlated with lower intensity
25 of the mHTT signal in the nucleoplasm (**Fig. 2C**). This loss of diffuse nucleoplasmic mHTT
26 was confirmed by an independent approach using immunohistochemistry with the EM48
27 antibody (**Supplementary Fig. 2C-E**).
28 To further investigate whether nucleolar stress results in a more severe Huntington-like

1 phenotype, we examined behavioral paradigms related to HD in control, TIF-IA^{D1Cre}, in R6/2
2 and in TIF-IA^{D1Cre}; R6/2 double mutant mice at 9, 10 and 11 weeks (**Fig. 2D,E**). At 10 weeks,
3 the double mutant mice performed significantly worse than the R6/2 mice, showing a more
4 severe deficit in coordinating gait changes with increasing acceleration (**Fig. 2D**). In line with
5 these results, at 10 weeks the double mutants performed less well in the forelimbs grip
6 strength test, in comparison to all other groups (**Fig. 2E**).

7 These results indicated that NPM1 and NCL are differentially perturbed, and the pattern of
8 mHTT accumulation points to a more advanced neuropathology in the double mutant mice.

9

10 **Reduced nucleolar localization of nucleophosmin 1 in the striatum of the late-onset** 11 **zQ175 mouse model of Huntington's disease**

12 To monitor nucleolar activity and integrity in a gradually progressing model of Huntington's
13 disease, we analyzed heterozygous zQ175 knock-in mouse model of Huntington's disease at
14 pre-symptomatic (5 months) and symptomatic ages (10 month) (Carty N *et al.*, 2015;
15 Menalled LB *et al.*, 2012). At 5 months, body weight and motor behavior of zQ175
16 heterozygous mice were comparable to that of control littermates (**Supplementary Fig. 3A-**
17 **C**). In line with a more advanced disease stage, both dopamine D2-receptor (*D2r*) and D1-
18 receptor (*D1r*) mRNAs were decreased at 10 months (**Fig. 3A**) (Menalled LB *et al.*, 2012).
19 Percentage of nuclei showing mHTT inclusions, area of the mHTT inclusions, and relative
20 mHTT intensity in the nucleoplasm and in the inclusions confirmed the more advanced
21 neuropathological stage at 10 months in comparison to 5 months in zQ175 mutant mice (**Fig.**
22 **3B-F** and (Carty N *et al.*, 2015)). By qRT-PCR assays, RNA in situ hybridization (ISH) and
23 Northern blots, we did not detect any significant differences in the 47S pre-rRNA, and mature
24 18S and 5.8S rRNA, indicating that rDNA transcription and mature rRNA *per se* are not
25 impaired in the striatum of zQ175 mice at the two considered stages (**Fig. 4**).

26 The analysis of human BA4 cortex RNAseq data (GSE79666)(Lin L *et al.*, 2016) and data
27 from the striata and gastrocnemius of zQ175 mice at different ages (HDinHD.org)(Langfelder
28 P *et al.*, 2016) shows dysregulation of genes involved in rRNA transcription and pre-rRNA

1 processing in this model at about 6 months (**Supplementary Fig. 3D,E**). These observations
2 along with the close interaction of mHTT with the nucleolus identified by immunofluorescence
3 co-localization of NCL with mHTT in the zQ175 model (**Fig. 3C**), led us to investigate
4 changes in NPM1 nucleolar protein re-distribution (**Fig. 5**). We analyzed the nucleolar
5 distribution of NCL and NPM1 proteins by confocal microscopy, in the striatum of zQ175
6 mice at 5 and 10 months. The number of DAPI positive nuclei showing a distinct NPM1
7 nucleolar staining was significantly reduced (ca. 40% less, $p=0.02$) in striatal neurons of
8 zQ175 mice at 5 months (**Fig. 5A, C**). At 10 months, a ca. 20% reduction was observed,
9 however it was not statistically significant ($p= 0.15$) (**Fig. 5A, C**). Similar to the Q111/111
10 cells and R6/2 mice, we found no evidence for change of NCL in the zQ175 mice (**Fig. 5B,**
11 **C**). To further investigate the spatial distribution of NPM1 with respect to the mHTT nuclear
12 foci, we performed super resolution microscopy in the striatum of zQ175 mice (STED, **Fig.**
13 **5D**). We observed a close proximity between diffuse nucleoplasmic NPM1 and mHTT that
14 appear intermingled at 5 months (**Fig. 5D, upper panels**), while at 10 months, mHTT was
15 mostly in the nuclear inclusion body (**Fig. 5D, lower panels**), showing that re-distribution of
16 nucleolar NPM1 precedes the formation of irreversible mHTT aggregates.
17 In summary, our results from striatal neurons in different models of Huntington's disease
18 identify nucleolar stress as a mechanism exacerbating disease progression, and NPM1 re-
19 distribution as a marker for disease progression and mHTT aggregation.

20

21 **Reduced nucleolar localization of NPM1 in skeletal muscle of zQ175 mice**

22 To explore the hypothesis that perturbed nucleolar homeostasis detected in the striatum by
23 NPM1 nucleolar mislocalization represents a histopathological marker of Huntington's
24 disease progression, we analyzed skeletal muscle (quadriceps) of controls and zQ175 mice
25 at 5 and 10 months (**Fig. 6A-C**). At 5 months the number of DAPI positive nuclei showing
26 either NPM1 or NCL signal was similar between zQ175 and control mice (**Fig. 6B**). The area
27 of the nuclei was also similar between control and zQ175 mutant mice at 5 and 10 months
28 (**Supplementary Fig. 4A, B**). However, in 10-month-old zQ175 mice, the nuclear area

1 displaying NPM1 immunosignal was about 30% decreased (**Fig. 6C**). Importantly, this
2 reduction was specific, as it was not observed for NCL (**Fig. 6C**). These findings suggest a
3 nucleolar phenotype in skeletal muscle of zQ175 mice at 10 months. As a read-out for
4 altered nucleolar function, we analyzed if rRNA synthesis was altered in skeletal muscle of
5 zQ175 mice. We studied pre-rRNA transcription and mature 18S rRNA by qRT-PCR, and we
6 detected at 10 months a significant (~50%) decrease of 47S pre-rRNA in skeletal muscle of
7 the zQ175 mice, in line with altered nucleolar function (**Fig. 6D**).

8 Next, we asked whether the changes in NPM1 signal in skeletal muscle of zQ175 mice at 10
9 months were secondary due to a compromised function of striatal neurons, or whether they
10 were associated with mHTT expression in the skeletal muscle. To this end, we analyzed
11 skeletal quadriceps muscle from the TIF-IA^{D1Cre} mouse model, characterized by massive
12 death of *D1r*-expressing medium spiny neurons at 3 months triggered by genetic induction of
13 nucleolar stress in these neurons (Kreiner G *et al.*, 2013). In this mHTT independent model
14 of striatal neurodegeneration, nuclear NPM1 signals were not reduced but rather significantly
15 elevated in skeletal muscle, compared to control littermate mice. These data suggest that the
16 reduced NPM1 signal observed in the skeletal muscle of the zQ175 mice is linked to the
17 peripheral effects of mHTT rather than to the degeneration of striatal neurons
18 (**Supplementary Fig. 4D,E**).

19

20 **Reduced nucleolar localization of NPM1 in skeletal muscle biopsies of Huntington's** 21 **disease patients**

22 For the critical transition of our findings from Huntington's disease mouse models to the
23 human disease, we analyzed skeletal muscle biopsies from Huntington's disease patients
24 and control individuals. More precisely, we investigated the NPM1 and NCL fluorescence
25 signal patterns in quadriceps muscle from biopsies of non-affected controls, pre-symptomatic
26 and early-symptomatic Huntington's patients (**Fig. 7A-C**). Details about the gender, age at
27 biopsy and length of the CAG repeat of the donors of muscle biopsies are provided in

1 **Supplementary Table 1.** We analyzed the percentage of DAPI positive nuclei showing
2 nucleolar NPM1 or NCL respectively, and the area of the NPM1 and NCL signal, similar as in
3 the zQ175 mice. In addition, we established an automated approach to quantify NPM1
4 immunofluorescence signals, as a prerequisite for future systematic high-throughput
5 histopathological assessments using NPM1 protein-distribution as a marker for disease
6 progression.

7 The images were first analyzed manually. Indeed, in early HD patients, the percentage of
8 DAPI positive nuclei showing nucleolar NPM1, and also the area of the NPM1 signal were
9 about 2- and 1.5-fold lower than those of controls, respectively (**Fig. 7B, C**). In the pre-HD
10 cohort, we observed a non-significant trend for reduced signals ($p=0.14$). A similar analysis
11 performed for NCL showed no differences in these parameters at any stage (**Fig. 7B, C**).
12 Nuclear areas were similar in all groups (**Supplementary Fig. 4C**).

13 The same images were reanalyzed with an optimized automated approach based on the
14 semantic convolutional neural network (CNN) learning, as indicated in the Materials and
15 Method section. This analysis delivered similar results. Moreover, manually derived and
16 automatically determined data displayed a strong correlation (**Supplementary Fig. 4F**). This
17 automated approach represents a prerequisite for using NPM1 distribution in skeletal muscle
18 as a marker for HD progression, and it opens the possibility to apply this analysis on a large
19 scale of samples by digital pathology.

20

1 Discussion

2 Nucleolar stress is associated with mHTT expression, and it is implicated in the response to
3 cellular stress and in protein quality control. In this study, we provided the first *in vivo*
4 evidences that this mechanism exacerbates motor phenotypes in a preclinical mouse model
5 of HD, and that it alters mHTT intranuclear distribution. Aberrant rRNA processing in a
6 striatal-derived cell model that expresses human mHTT indicated a novel mHTT-associated
7 intrinsic dysfunctional mechanism. As summarized in the **Supplementary Table 2**, the
8 nucleolar localization of the protein NPM1 was specifically reduced in the skeletal muscles of
9 HD mice and in biopsies from HD patients, suggesting a novel candidate histopathological
10 biomarker for monitoring HD progression in a peripheral tissue.

11 These findings are particularly important because changes in NPM1 distribution appear to be
12 required for maintaining mHTT in a disperse state in the nucleoplasm. NPM1 and mHTT are
13 known to interact (Culver BP *et al.*, 2012; Shirasaki DI *et al.*, 2012). NPM1 contains
14 disordered and low-complexity sequences that may render this protein prone to interact with
15 mHTT. Recent evidence showed that mHTT has distinct dynamic states in living cells,
16 including fast diffusion rates, dynamic clustering and stable aggregation (Peskest TR *et al.*,
17 2018). Studies in HEK293T cells transfected with artificial beta-sheet proteins, mimicking
18 prefibrillar and fibrillar aggregate formation suggested that NPM1 might shield mHTT
19 aggregate surface (Woerner et al, Science 2016). Our finding that the disruption of nucleolar
20 integrity, and NPM1 release from the nucleolus, promote the loss of a diffuse mHTT state
21 reconciles with the role of nucleolar integrity in protein quality control and formation of
22 irreversible protein aggregates (Amer-Sarsour F and Ashkenazi A, 2019; Banski P *et al.*,
23 2010; Frottin F *et al.*, 2019; Nollen EA *et al.*, 2001).

24 Previous studies showed that NPM1 is transiently upregulated in striatal neurons of the R6/2
25 transgenic mice before worsening of motor endpoints (Pfister JA and D'Mello SR, 2016), and
26 that its nucleolar localization is partially lost in the same model at a pre-symptomatic stage
27 (Kreiner G *et al.*, 2013). Accordingly, the zQ175 mice show that NPM1 nucleolar localization

1 is partially lost at a pre-symptomatic stage, further corroborating that changes in NPM1
2 subcellular distribution might be pathogenic. These findings are in agreement with the
3 biphasic nature of nucleolar stress observed for example in amyotrophic lateral sclerosis
4 (ALS). In this condition nucleolar stress occurs before the typical TDP-43 (TAR DNA-binding
5 protein 43) proteinopathy (Aladesuyi Arogundade O *et al.*, 2021).

6 In turn, mHTT interaction with NPM1 might exert toxicity by affecting the multiple functions of
7 NPM1. On the other hand, other pathogenic effects can be hypothesized. NPM1 impairment
8 leads to an accumulation of pre-rRNA and various processing intermediates, as shown by
9 NPM1 depletion experiments in human cells (Tafforeau L *et al.*, 2013). While NPM1
10 knockdown is toxic, its nuclear overexpression protects against mHTT-induced death in
11 cultured cerebellar granule and cortical neurons (Pfister JA and D'Mello SR, 2016). We
12 showed that the expression of human mHTT in striatal-derived cells is associated with
13 qualitative alterations of ribosome production, namely the activation of cryptic processing
14 sites, and that NPM1 loses its nucleolar distribution in the same model. At this stage, we
15 cannot rule out that altered NPM1 affects pre-rRNA processing or sorting, as reported for
16 another nucleolar protein fibrillarin in human cell cultures (Yao RW *et al.*, 2019). Future
17 studies should address whether such changes in the kinetics of RNA cleavage impact other
18 facets of ribosome biogenesis, such as rRNA modifications or pre-ribosome assembly, and
19 result in the production of ribosomes with altered translational abilities. Interestingly, in a
20 genome-wide screen in yeast, expression of a mutant huntingtin fragment (Htt103Q) causes
21 a dramatic reduction in expression of genes involved in rRNA metabolism and ribosome
22 biogenesis (Tauber E *et al.*, 2011). Moreover cells expressing HttQ138 show a decreased
23 translation by the prion-like protein and translation regulator Orb2, sequestered by mHTT
24 aggregates (Joag H *et al.*, 2019). Recently, mHTT has been reported to suppress protein
25 synthesis in the same HD cell model adopted here by a mechanism involving ribosome
26 stalling (Eshraghi M *et al.*, 2021). Increased translation has been however reported in a
27 different progressive transgenic model of Huntington's disease (Creus-Muncunill J *et al.*,
28 2019). The phosphorylation of the eukaryotic translation initiation factor 4E (eIF4E) binding

1 protein (4E-BP), an inhibitor of translation, increases in the striatum of R6/2 mice at a late
2 manifest stage, supporting a time-specific dysregulation of translation (Creus-Muncunill J *et*
3 *al.*, 2019).

4 Our findings point not only to nucleolar stress as a contributor to Huntington's disease, but
5 also to re-distribution of nucleolar NPM1 as a cellular marker for Huntington's disease
6 progression. As summarized in **Supplementary Table 2**, there are tissue-specific
7 differences within the same model (striatum vs. skeletal muscle), model-specific differences
8 within the striatum (R6/2 vs. zQ175 mice) and age-specific differences within the muscle
9 (zQ175 at 5 and 10 months) for nucleolar transcription and integrity. It remains to be
10 analyzed whether these differences in nucleolar function and integrity correlate with different
11 levels and / or state of mHTT (fibrils vs. inclusion bodies) and/or NPM1. These studies will be
12 also important for the validation of NPM1 as a histopathological biomarker in longitudinal
13 studies and for testing beneficial and adverse effects of therapeutic intervention on HD
14 progression. In cancer research, changes in nucleolar size and shape are considered a
15 reliable parameter to predict tumor growth and nucleolar proteins are evaluated as
16 therapeutic targets (Derenzini M *et al.*, 2000; Montanaro L *et al.*, 2008; Nunez Villacis L *et*
17 *al.*, 2018). However, the value of the nucleolus as a potential biomarker is still neglected in
18 the field of neurodegenerative diseases. We showed here, as a proof of principle, how the
19 analysis of NPM1 could be automatized for clinical neuropathology applications, paving the
20 way for high-throughput systematic analysis. A shared role for nucleolar stress in progressive
21 neurodegenerative disorders, characterized by accumulation of intranuclear inclusions awaits
22 future investigations (Amer-Sarsour F and Ashkenazi A, 2019; Latonen L, 2019; Lee KH *et*
23 *al.*, 2016; Rekulapally P and Suresh SN, 2019). The cell-specific and progressive modeling
24 of nucleolar stress by using the TIF-1A conditional ablation is an important tool to investigate
25 *in vivo* the early molecular, cellular, and behavioral responses to the loss of nucleolar
26 homeostasis in genetic and pharmacological animal models (Domanskyi A *et al.*, 2011;
27 Evsyukov V *et al.*, 2017; Kreiner G *et al.*, 2013; Rieker C *et al.*, 2011; Vashishta A *et al.*,
28 2018).

1 In conclusion, we identified nucleolar stress as a disease mechanism contributing to HD
2 pathogenesis, and in particular NPM1 distribution pattern in skeletal muscle as a novel
3 promising candidate for developing an accessible and reliable biomarker for Huntington's
4 progression and possibly a target for therapeutics.
5

1 **Materials and Methods**

2 **Statement regarding the ethical use of human material and animals**

3 The ethics committee at Ulm University approved the study (Protocol number: 165/12), and
4 written informed consent was obtained from each participant.

5 Procedures involving animal care and use were approved by the Committee on Animal Care
6 and Use (Regierungspräsidium Karlsruhe, Germany, Animal Ethic Protocols: 34-9185.81/G-
7 297/14 and 35-9185.81/G-102/16) in accordance with the local Animal Welfare Act and the
8 European Communities Council Directives (2012/707/EU).

9

10 **Human skeletal muscle biopsies**

11 Ten *HTT* CAG trinucleotide repeat expansion carriers and five healthy sex- and age-matched
12 controls were recruited at the Department of Neurology of Ulm University (**Supplementary**
13 **Table 1**). Participants had no contra-indications to muscle biopsy, e.g. a clotting disorder or
14 abnormalities on electrocardiograms. *HTT* CAG repeat length was determined and
15 participants were clinically assessed as described for the TrackOn and TRACK-HD studies
16 (Orth M *et al.*, 2017; Tabrizi SJ *et al.*, 2009). The disease burden score (DBS) was calculated
17 from each Huntington's disease participant's CAG repeat length and age according to the
18 following formula: $(\text{CAG} - 35.5) \times \text{age}$ (Penney JB, Jr. *et al.*, 1997). Clinical assessment
19 included the United Huntington's Disease Rating Scale (UHDRS) motor part to derive the
20 total motor score (TMS) (Group THsDCR, 1993) and the UHDRS total functional capacity
21 scale (TFC). Potential Huntington's disease participants were screened if they had a disease
22 burden score of 250 or greater and either had no clinical signs of manifest motor
23 Huntington's disease (preHD) or were in TFC stages of 1 or 2 indicative of early motor
24 manifest Huntington's disease (earlyHD). **Supplementary Table 1** summarizes the
25 participant demographic, number of CAG repeat, disease burden and UHDRS total motor
26 score data.

27 Open biopsies of the *M. vastus lateralis* were obtained following local anesthesia. For
28 immunofluorescence muscle was mounted on a piece of cork in TissueTek with fibers

1 oriented perpendicular to the cork and then snap-frozen in liquid N₂-cooled 2-methylbutane
2 and stored at -80°C until sectioning.

3

4 **Mice**

5 B6CBA-Tg(HDexon1)62Gpb/1J (R6/2) transgenic mice (CAG160) were imported from the
6 Jackson Laboratories (Bar Harbour, ME). *Htt*^{tmtm1^{Mfc}}/190tChdi (zQ175 knock-in) mice
7 (CAG198) were received from the CHDI Foundation by the Jackson Laboratories. For the
8 experiments reported here, male and female mice were used, and wild-type and mutant
9 littermates were analyzed. The zQ175 knock-in mice carry ca. 190 CAG repeats in a
10 chimeric human/mouse exon 1 of the murine *Htt* gene (Menalled LB *et al.*, 2012). The zQ175
11 mutation was kept in heterozygosity, to limit toxicity and mimic the most common genetic
12 condition in Huntington's disease (Menalled LB *et al.*, 2012). The conditional knock-out of the
13 nucleolar transcription factor *Tif-1a* gene by the Cre-LoxP system in dopamine receptor 1
14 (D1R)-expressing cells (official nomenclature: B6.129.FVB/N-TIF-1A^{tm^{GSc}}-Tg(D1RCre)^{GSc},
15 abbreviated as TIF-1A^{D1Cre}) was achieved as previously described (Kreiner G *et al.*, 2013).
16 Based on our breeding scheme crossing triple heterozygous mice with homozygous floxed
17 *Tif-1a* mice, we obtained 1 out of 8 R6/2 transgenic mice with the conditional loss of *Tif-1a*.
18 Mice were housed in a standard 12-h light/dark cycle and kept with ad libitum access to food
19 and water. The analysis of the genotype was performed by PCR of tail snips as previously
20 described (Kreiner G *et al.*, 2013; Levine MS *et al.*, 1999; Naranjo JR *et al.*, 2016).

21

22 **Behavioral tests**

23 Mice were tested for motor function on a rotarod apparatus (Ugo Basile, Gemonio, Italy)
24 using a gradual acceleration protocol (4–40 rpm) up to maximal 8 min. Forelimb strength of
25 all experimental groups was tested using a grip strength meter (Ugo Basile, Gemonio, Italy,
26 model 47106), which automatically measured the force needed for the mouse to release its
27 grip (Neureither F *et al.*, 2017).

1 Rotarod and grip strength tests were performed 2 days after adapting to the respective tests
2 at 9 weeks (trial 1), at 10 weeks (trial 2) and at 11 weeks (trial 3) for the experimental groups
3 including control, TIF-IA^{D1Cre}, R6/2 and their double mutant mice, and on the next day for the
4 experimental groups including control and zQ175 mice (5 month-old). On the day of each
5 trial each mouse was tested three times in intervals of 15 min. The mean endurance for the
6 three runs (or recorded force, in millinewton) per mouse was calculated. The tests were
7 performed blind for genotype.

8

9 **Tissue processing for RNA extraction and quantitative real-time PCR (qRT-PCR) in** 10 **mice**

11 Total RNA was isolated from dissected mouse striatum in the region comprised between
12 Bregma 1.34 mm and -0.34 mm (Franklin P, 2008). Synthesis of complementary DNA
13 (cDNA) with M-MLV Reverse Transcriptase (SuperScript III First Strand Synthesis Supermix,
14 18080-400, Thermo Scientific) was primed with random hexamers. For detection of pre-
15 rRNA, either the first 130 nucleotides relative to the transcription start site (47S 1) were
16 amplified using the 5'-ACTGACACGCTGTCCTTTCC and 5'-GACAGCTTCAGGCACCGCGA
17 primers or a primer pair covering the first processing site (47S 2) was used: 5'-
18 CGTGTAAGACATTCCTATCTCG and 5'-GCCCGCTGGCAGAACGAGAAG. To detect
19 *Gapdh* mRNA (Glyceraldehyde 3-phosphate dehydrogenase) we used the following primers:
20 5'-CATGGCCTTCCGTGTTCTTA and 5'-GCGGCACGTCAGATCCA. Pre-rRNA and *Gapdh*
21 mRNA amplification was performed using SYBR GREEN chemistry (SsoAdvanced Universal
22 SYBR Green Supermix, 1725271, Bio-Rad), as previously described (Kiryk et al, 2013). The
23 TaqMan gene expression assays (ThermoFischer Scientific) used for this study are reported
24 in **Supplementary Table 3**. For each amplicon serial dilutions of cDNA were included in
25 each run by a StepOnePlus instrument (Applied Biosystems) to generate standard curves
26 that were used for relative expression quantification. Pre-rRNA expression in the striatum
27 was normalized using the stably expressed reference gene *Gapdh* (glyceraldehyde-3-
28 phosphate dehydrogenase), while for the TaqMan assays we used the stably expressed *Hprt*

1 (hypoxanthine-guanine phosphoribosyl transferase) for striatal tissue and *Metap1*
2 (methionine aminopeptidase 1) (Hering T *et al.*, 2015; Hering T *et al.*, 2017) for muscle
3 tissue. Changes in relative expression were calculated as a fold change versus mean of
4 respective control samples. All experiments were performed blind for genotype.

5

6 **Tissue processing for immunostaining in mouse and human tissues**

7 Mice were sacrificed by cervical dislocation and brains and skeletal muscle (quadriceps)
8 were immediately dissected. For immunofluorescence and immunohistochemistry, one brain
9 hemisphere was fixed in 4% paraformaldehyde (PFA) in phosphate-buffered saline (PBS),
10 pH7.4 overnight at 4 °C and paraffin embedded. Coronal sections (7 µm) were cut on a
11 microtome (Leica 2235). The region of the striatum comprised between Bregma +0.74 mm
12 and -0.34 mm was used for the histological analyses. Mouse skeletal muscle (quadriceps)
13 was mounted on a piece of cork in Tissue Freezing Medium (12020108926, Leica) with fibers
14 oriented perpendicular to the cork and then snap-frozen in liquid N₂-cooled 2-methylbutane
15 and stored at -80°C until sectioning. Sections were cut in transverse orientation to the fiber
16 direction at 12 µm using a Leica CM1859 cryostat. Cryosections were fixed in 4% PFA for 15
17 min before staining. For antigen retrieval the slides were boiled in 1X citrate buffer (HK086-
18 9K, Biogenex) for 3 min at 800 W in a microwave and then for 8 min at 400 W. Sections were
19 blocked with 5% normal swine serum (NSS, S-4000, Vector) for 30 min. Primary antibodies
20 were diluted in 5% NSS and incubated over night at 4°C in a humidified chamber. For
21 immunohistochemistry, visualization of antigen-bound primary antibodies was carried out
22 using a biotinylated secondary antibody together with the avidin-biotin system and the
23 VECTOR peroxidase kit (PK-6100, Vector Laboratories) using both diaminobenzidine tablets
24 (D4293, Sigma) as a substrate. Fluorescent-dye conjugated secondary antibodies were
25 added and incubated for 30 min at room temperature. For double immunofluorescence
26 staining, slides were incubated with a second primary antibody as described before. Nuclei
27 were stained with DAPI (4',6-diamidino-2-phenylindole) (1:10⁶, 62248, Invitrogen) for 10 min
28 at room temperature. Slides were mounted using AquaPolymount (18606-20, Polysciences)

1 and stored in the dark at 4°C until microscopic analyses. Primary antibodies for
2 immunostaining were: anti-nucleolin (NCL, 1:500, ab70493, abcam) (Evsyukov V *et al.*,
3 2017; Potapova TA *et al.*, 2019), anti-nucleophosmin 1 (NPM1/B23, 1:100, MAB4500,
4 Millipore) (Parlato R *et al.*, 2006; Wang HF *et al.*, 2011), sequestosome 1 (p62/SQSTM1)
5 (1:100, P0067, Sigma), EM48 (1:100, MAB5374, Millipore) (Davies SW *et al.*, 1997), S830
6 (1:1000; Neueder/Bates) (Moffitt H *et al.*, 2009). For confocal microscopy, secondary
7 antibodies Alexa 488 (A-21206, 1:100, Thermo Scientific) and Alexa 594 (A-21207, 1:100,
8 Thermo Scientific) were used. For stimulated emission depletion (STED) microscopy, Alexa
9 594 (A-21207, 1:100 Thermo Scientific) and Star Red (STAR-RED-1056, 1:100 Abberior
10 GmbH) were used.

11

12 **Mouse cell tissue culture conditions**

13 The StHdh Q7/Q7, Q7/Q111, Q111/Q111 cells (striatal neuronal derived from Hdh7 wild-type
14 and Hdh111 knock-in mice) (Trettel F *et al.*, 2000) were cultured in Dulbecco's modified
15 Eagle's medium medium (SIGMA) supplemented with Glutamax (GIBCO) and 10%
16 inactivated fetal bovine serum (GIBCO) at 5% CO₂ (Naranjo JR *et al.*, 2016).

17

18 **Pre-rRNA processing analysis**

19 5 µg total RNA from the StHdh Q7/Q7, Q7/Q111, Q111/Q111 cells (80% confluent grown in
20 Petri dishes 6 mm diameter) was extracted, separated by 1.2% denaturing gel
21 electrophoresis and processed for Northern blotting according to (Tafforeau L *et al.*, 2013).
22 The probe used was LD4098 (5'-ETS_A0-1, ACAATGACCACTGCTAGCCTCTTTCCCTT).
23 Panels D and F were migrated at 60 V for 16 h; panel E, at 65 V for 24 h. The 28S/18S ratios
24 were extracted from electropherograms (Agilent, RNA 6000 Nano Kit #5067-1511).

25

26 **Northern blot for 5.8S rRNA analysis**

27 RNA was extracted from the entire striatum of one mouse brain hemisphere using the Trizol
28 method (Invitrogen). 1-3µg were separated using 15% urea-PAGE (Invitrogen). Gels were

1 stained with SYBR Gold (Invitrogen), and immediately imaged and transferred to Nytran
2 SuperCharge membranes (Schleicher and Schuell), and UV crosslinked with an energy of
3 0.12 J. Membranes were hybridized in 5X SSC, 20mM Na₂HPO₄, pH7.4, 7% SDS, 1X
4 Denhardt's for at least 1 h at 42°C. For detection of 5.8S and 5S rRNA, membranes were
5 incubated overnight (12–16 h) at 42°C with ³²P-end-labelled oligonucleotides probes added
6 in hybridization buffer with following sequence: 5.8S: 5'-GATGATCAATGTGTCCTGCAAT-3';
7 5S: 5'-GGGTGGTATGGCCGTAGAC-3'. Following overnight incubation, the membranes
8 were washed for 15 min at 43°C with 3X SSC, 5% SDS and for 15 min at room temperature
9 with washing buffer (1X SSC, 1% SDS). Membranes were exposed on film, then stripped
10 and re-hybridized with 5S probe for further analysis. Quantification of Northern blot signals
11 from three independent experiments was performed on autoradiographs using Fiji/ImageJ
12 (Schindelin J *et al.*, 2012).

13

14 **RNA in situ hybridization for quantification of RNA foci**

15 Non-radioactive RNA *in situ* hybridization (ISH) was performed on four to eight paraffin
16 sections per mouse using a specific riboprobe hybridizing to regions in the leader sequence
17 of the pre-rRNA as previously described (Rieker C *et al.*, 2011). In brief after paraffin
18 removal, sections were rehydrated and treated with proteinase K (10 µg/ml in 20 mM
19 Tris/HCl, 1 mM EDTA, pH 7.2) for 7 min. Sections were incubated for 30 min in 2X SSC and
20 in Tris/glycine buffer for at least 30 min until application of the hybridization mixture. The
21 hybridization mixture was prepared as follows: 40% deionized formamide (Life Technologies,
22 USA), 5X SSC, 1X Denhardt's solution (Invitrogen, USA), 100 mg/ml salmon sperm DNA,
23 100 mg/ml yeast tRNA, 50 – 100 ng riboprobe, diluted in DEPC-H₂O to a final volume of 100
24 µl per slide. Slides were incubated at 55 °C overnight. Post-hybridization steps were
25 performed by washing the slides in 0.5X SSC/20% formamide at 60 °C and in NTE (0.5M
26 NaCl, 10 mM Tris pH 7.0, 5 mM EDTA) at 37 °C. Slides were then incubated with 10 µg/ml
27 RNase A in NTE for 30 min at 37 °C. Samples were washed in pre-warmed 0.5X SSC/20%
28 formamide for 30 min at 60 °C and kept in 2X SSC for 30 min at room temperature. Sections

1 were then placed in blocking solution (1 % blocking reagent, 11096176001, Roche, diluted in
2 100 mM maleic acid, 150 mM NaCl, pH 7.5) for 10 min at room temperature. Subsequently,
3 sections were incubated with alkaline phosphatase-conjugated anti-digoxigenin antibody
4 overnight at 4 °C. NBT/BCIP liquid substrate system for alkaline phosphatase
5 (11681451001, Roche) was used for the staining reaction at room temperature in the dark.
6 Incubation was stopped after 4 – 5 h. Sections were counterstained for 10 min with Nuclear
7 Fast Red (Vector Laboratories, USA), and subsequently the coverslip was mounted with
8 Kaiser's Glycerol Gelatin (Merck, Germany). In situ hybridization and immunohistochemistry
9 images were acquired by a Leica DM6B microscope with a DMC2900 camera using a 20X
10 objective.

11

12 **Polysome profiling**

13 5×10^6 StHdh Q7/Q7 and Q111/Q111 cells were treated with cycloheximide (100 µg/ml) for 5
14 min and washed once in cold PBS/cycloheximide (100 µg/ml). The cells were lysed in 400µl
15 lysis buffer (15 mM Tris–HCl, pH 7.4, 15 mM MgCl₂, 300 mM NaCl, 1% Triton X-100, 100
16 µg/ml cycloheximide, 1X complete protease inhibitors (Roche), 0.1% β-mercaptoethanol). As
17 RNase inhibitor we used RNasin (200U/ml) (Thermo Fisher Scientific). The lysates were
18 centrifuged at 10,000 g for 10 min at 4 °C, and the supernatants were applied to linear 17.5–
19 50% sucrose gradients in 20 mM Tris–HCl (pH 7.4), 5 mM MgCl₂, and 150 mM NaCl.
20 Centrifugation was carried out at 36,000 rpm for 2.5 h at 4°C in a Beckmann SW60 rotor.
21 Gradients were eluted with an ISCO UA-6 gradient fractionator, and polysome profiles were
22 recorded by continuously monitoring the absorbance at 254 nm. The fraction of ribosomes
23 engaged in translation was calculated by dividing the area under the polysomal part of the
24 curve by the total area.

25

26 **SURface SEnSING of Translation (SUnSET) assay**

27 StHdh Q7/Q7 and Q111/Q111 cells (90% confluent grown in Petri dishes 6 cm diameter) The
28 cells were incubated with 1µg/ml of puromycin for 30min and then analyzed to detect the

1 puromycin-labeled peptides by immunoblotting. The puromycin concentration was
2 determined by preliminary experiments of cell viability at 0.1-1.5 µg/ml. For immunoblotting
3 total extracts were prepared by re-suspending cells in RIPA buffer (25 mM Tris-HCl pH 7.6,
4 150 mM NaCl, 5 mM EDTA (Ethylenediaminetetraacetic acid), 1% Triton, 1% sodium
5 deoxycholate, 0.1% SDS), 1 mM PMSF (phenylmethylsulfonyl fluoride), 1 mM DTT
6 (Dithiothreitol), 1X proteinase inhibitor (ROCHE complete, EDTA free). Protein quantification
7 was performed by using the Thermo Scientific Pierce BCA protein Assay kit (detergent
8 compatible formulation). The whole extracts (20 µg) were loaded on 10% SDS-PAGE gel
9 and blotted on PVDF (Polyvinylidene fluoride) membrane (Biorad) with wet apparatus
10 (Biorad), for 60 min at 400 mA. After blocking in 5% dry milk in TBS, the membrane was
11 incubated overnight with the appropriate primary antibodies. The primary antibodies used
12 were: anti-puromycin (Millipore MABE343, 1:1000) and anti-beta actin (sc-47778, Santa Cruz
13 Biotechnology, 1:1000). The secondary antibody was anti-mouse HRP (horseradish
14 peroxidase)-linked (NA931, Amersham ECL Mouse IgG, HRP, GE Healthcare Life Science)
15 diluted 1:10000 in 5% dry milk in PBS, and incubated for 1h at room temperature. After ECL
16 (Electrochemiluminescence) assay (Pierce ECL Western Blotting Substrate cat. 32106
17 Thermo Fisher Scientific), the membrane was incubated with the film (Kodak) for protein
18 detection. As additional loading control, the same amount of total protein extracts were
19 loaded on 10% SDS-PAGE and then stained with Coomassie Blue R-250 (Sigma). Protein
20 expression was quantified by densitometric analysis with the ImageJ Software.

21

22 **Confocal and STED super-resolution microscopy**

23 Confocal images of the striatum and muscle sections were obtained as z-stacks using a
24 confocal scanning microscope (Leica TCS SP8) with a 63X/1.32NA oil objective and Leica
25 LAS X imaging software. STED images were acquired as z-stacks in 0.5 µm steps at the
26 Stedycon (Abberior Instruments GmbH) with a 100X/1.4NA oil objective. STED images were
27 deconvoluted by the Huygens software (Scientific Volume Imaging, Hilversum, The
28 Netherlands).

1 **Image analysis**

2 All microscopic images were analyzed by an experimenter blinded to the genotype and age
3 using the Fiji software (Schindelin J *et al.*, 2012). The number and area of nucleolar markers
4 were analyzed, as previously described (Evsyukov V *et al.*, 2017; Kiryk A *et al.*, 2013;
5 Kreiner G *et al.*, 2013; Tiku V *et al.*, 2018). The percentage of nuclei showing NCL and
6 NPM1 in the nucleoli was determined by counting the number of DAPI positive nuclei
7 showing a circular nucleolar signal. The mean area of the nucleolar marker signal was
8 determined by circling the signal area in each DAPI positive nucleus, considering in total only
9 the double-labelled nuclei (Tiku V *et al.*, 2018). The percentage of DAPI positive nuclei
10 showing intranuclear mHTT inclusions and their mean area was measured in a similar way.
11 For the semi-quantitative analysis of the signal mean intensities, nuclei labelled with DAPI
12 were identified and marked in maximal projection images and the DAPI negative region
13 outside was considered as the background. A cut-off of $50 \mu\text{m}^2$ was applied to exclude
14 smaller fragmented DAPI positive signals. The DAPI positive area identified the region of
15 interest (ROI). The mean intensities of NCL in the entire nucleus and the respective
16 background were measured in each of the 10 planes of the z-stack, and the intensities of
17 every plane were summed up. The intensity of the signal in the ROI was subtracted by the
18 background intensity for each nucleus. The relative mHTT subcellular distribution was
19 defined by the ratio between mHTT mean intensities in and outside the nucleus (Gasset-
20 Rosa F *et al.*, 2017). The intranuclear distribution was defined as the ratio between mHTT
21 intensity in the nucleoplasm and in the inclusions (Frottin F *et al.*, 2019). The region of the
22 nucleus not occupied by the mHTT inclusions was considered as the nucleoplasm. For this
23 analysis the mHTT inclusions were marked on the maximal z-projection. Intensities were
24 measured across the whole z-stack and summed up. For each nucleus the intranuclear
25 mHTT distribution was calculated by dividing the mHTT intensity in the nucleoplasm by the
26 mHTT intensity in the inclusion.
27 For the quantification of the number of pre-rRNA foci by in situ hybridization the signals
28 produced by labeling the riboprobe with digoxigenin were counted and normalized to the

1 number of nuclei identified by counterstaining with the Nuclear Fast Red, as previously
2 reported (Evsyukov V *et al.*, 2017).

3 The manual segmentation of NPM1 positive nucleoli in human skeletal muscle biopsies was
4 automated by a semantic image segmentation algorithm based on deep learning. The neural
5 network used here is a fully convolutional neural network (FCN) using exclusively
6 convolutional operations and it can thus be applied to images of arbitrary size in a
7 computationally efficient way (Shelhamer E *et al.*, 2017). The detailed network architecture
8 used here was developed and provided by Wolution GmbH & Co. KG, through its scientific
9 image analysis platform, and it uses five convolutional layers as well as activation functions
10 of ReLu type. The power of such architectures for medical applications was previously
11 demonstrated (Havaei M *et al.*, 2017). The results of the percentage of NPM1 positive nuclei
12 and of the NPM1 signal area achieved by the manual and automated approach were then
13 correlated. Line profiles were measured after acquisition using ImageJ. A line through the
14 nucleolus was drawn and measured using the Plot Profile function, as previously described
15 (Riback JA *et al.*, 2020; Taslimi A *et al.*, 2014; Zhu L *et al.*, 2019).

16

17 **Statistics**

18 Statistical analysis was performed with Graphpad Prism 7.04 software. Mean values per
19 sample were used for statistical analysis. Datasets were analyzed for their statistical
20 significance using non-parametric unpaired, two-tailed Mann-Whitney U (MWU) test or using
21 the Kruskal-Wallis test followed by Dunn's post-hoc analysis for multiple comparisons
22 (Altman DG *et al.*, 1983). The MWU tests could not be applied for data shown in Fig. 4 due to
23 no variation of the data points for the control group. Behavioral data were analyzed by two-
24 way ANOVA with Tukey's post-hoc analysis. For all tests statistical significance level was set
25 at $p < 0.05$. Complete details about statistical analysis are provided as **Supplementary**

26 **Statistical Information.**

27

28

1 **Data availability**

2 The raw data that support the findings of this study are available under “Supplementary
3 statistical information” and from the corresponding author upon reasonable request.

4

1 **References**

- 2 Aladesuyi Arogundade O, Nguyen S, Leung R, Wainio D, Rodriguez M, and Ravits J
3 Nucleolar stress in C9orf72 and sporadic ALS spinal motor neurons precedes TDP-43
4 mislocalization. *Acta Neuropathol Commun* 2021; 9: 26.
- 5 Aladesuyi Arogundade O, Stauffer JE, Saberi S, Diaz-Garcia S, Malik S, Basilim H, *et al.*
6 Antisense RNA foci are associated with nucleoli and TDP-43 mislocalization in C9orf72-
7 ALS/FTD: a quantitative study. *Acta Neuropathol* 2019; 137: 527-530.
- 8 Altman DG, Gore SM, Gardner MJ, and Pocock SJ Statistical guidelines for contributors to
9 medical journals. *Br Med J (Clin Res Ed)* 1983; 286: 1489-1493.
- 10 Amer-Sarsour F, and Ashkenazi A The Nucleolus as a Proteostasis Regulator. *Trends Cell*
11 *Biol* 2019; 29: 849-851.
- 12 Banski P, Kodiha M, and Stochaj U Chaperones and multitasking proteins in the nucleolus:
13 networking together for survival? *Trends Biochem Sci* 2010; 35: 361-367.
- 14 Bates GP, Dorsey R, Gusella JF, Hayden MR, Kay C, Leavitt BR, *et al.* Huntington disease.
15 *Nat Rev Dis Primers* 2015; 1: 15005.
- 16 Boulon S, Westman BJ, Hutten S, Boisvert FM, and Lamond AI The nucleolus under stress.
17 *Mol Cell* 2010; 40: 216-227.
- 18 Caron NS, Dorsey ER, and Hayden MR Therapeutic approaches to Huntington disease: from
19 the bench to the clinic. *Nat Rev Drug Discov* 2018; 17: 729-750.
- 20 Carty N, Berson N, Tillack K, Thiede C, Scholz D, Kottig K, *et al.* Characterization of HTT
21 inclusion size, location, and timing in the zQ175 mouse model of Huntington's disease: an in
22 vivo high-content imaging study. *PLoS One* 2015; 10: e0123527.
- 23 Cong R, Das S, Ugrinova I, Kumar S, Mongelard F, Wong J, *et al.* Interaction of nucleolin
24 with ribosomal RNA genes and its role in RNA polymerase I transcription. *Nucleic Acids Res*
25 2012; 40: 9441-9454.
- 26 Consortium. GMoHsD CAG Repeat Not Polyglutamine Length Determines Timing of
27 Huntington's Disease Onset. *Cell* 2019; 178: 887-900 e814.
- 28 Creus-Muncunill J, Badillos-Rodriguez R, Garcia-Forn M, Masana M, Garcia-Diaz Barriga G,
29 Guisado-Corcoll A, *et al.* Increased translation as a novel pathogenic mechanism in
30 Huntington's disease. *Brain* 2019; 142: 3158-3175.

- 1 Culver BP, Savas JN, Park SK, Choi JH, Zheng S, Zeitlin SO, *et al.* Proteomic analysis of
2 wild-type and mutant huntingtin-associated proteins in mouse brains identifies unique
3 interactions and involvement in protein synthesis. *J Biol Chem* 2012; 287: 21599-21614.
- 4 Davies SW, Turmaine M, Cozens BA, DiFiglia M, Sharp AH, Ross CA, *et al.* Formation of
5 neuronal intranuclear inclusions underlies the neurological dysfunction in mice transgenic for
6 the HD mutation. *Cell* 1997; 90: 537-548.
- 7 Dayalu P, and Albin RL Huntington disease: pathogenesis and treatment. *Neurol Clin* 2015;
8 33: 101-114.
- 9 Derenzini M, Montanaro L, and Trere D What the nucleolus says to a tumour pathologist.
10 *Histopathology* 2009; 54: 753-762.
- 11 Derenzini M, Trere D, Pession A, Govoni M, Sirri V, and Chieco P Nucleolar size indicates
12 the rapidity of cell proliferation in cancer tissues. *J Pathol* 2000; 191: 181-186.
- 13 Domanskyi A, Geissler C, Vinnikov IA, Alter H, Schober A, Vogt MA, *et al.* Pten ablation in
14 adult dopaminergic neurons is neuroprotective in Parkinson's disease models. *FASEB J*
15 2011; 25: 2898-2910.
- 16 Drygin D, Rice WG, and Grummt I The RNA polymerase I transcription machinery: an
17 emerging target for the treatment of cancer. *Annu Rev Pharmacol Toxicol* 2010; 50: 131-156.
- 18 Eshraghi M, Karunadharma PP, Blin J, Shahani N, Ricci EP, Michel A, *et al.* Mutant
19 Huntingtin stalls ribosomes and represses protein synthesis in a cellular model of Huntington
20 disease. *Nat Commun* 2021; 12: 1461.
- 21 Evsyukov V, Domanskyi A, Bierhoff H, Gispert S, Mustafa R, Schlaudraff F, *et al.* Genetic
22 mutations linked to Parkinson's disease differentially control nucleolar activity in pre-
23 symptomatic mouse models. *Dis Model Mech* 2017; 10: 633-643.
- 24 Francelle L, Lotz C, Outeiro T, Brouillet E, and Merienne K Contribution of Neuroepigenetics
25 to Huntington's Disease. *Front Hum Neurosci* 2017; 11: 17.
- 26 Franklin P. *The mouse brain in stereotaxic coordinates*, 3d edn: Elsevier;2008.
- 27 Frottin F, Schueder F, Tiwary S, Gupta R, Korner R, Schlichthaerle T, *et al.* The nucleolus
28 functions as a phase-separated protein quality control compartment. *Science* 2019; 365:
29 342-347.

- 1 Gasset-Rosa F, Chillon-Marinas C, Goginashvili A, Atwal RS, Artates JW, Tabet R, *et al.*
2 Polyglutamine-Expanded Huntingtin Exacerbates Age-Related Disruption of Nuclear Integrity
3 and Nucleocytoplasmic Transport. *Neuron* 2017; 94: 48-57 e44.
- 4 Ghosh R, and Tabrizi SJ Clinical Features of Huntington's Disease. *Adv Exp Med Biol* 2018;
5 1049: 1-28.
- 6 Gomes C, Smith SC, Youssef MN, Zheng JJ, Hagg T, and Hetman M RNA polymerase 1-
7 driven transcription as a mediator of BDNF-induced neurite outgrowth. *J Biol Chem* 2011;
8 286: 4357-4363.
- 9 Group THsDCR A novel gene containing a trinucleotide repeat that is expanded and
10 unstable on Huntington's disease chromosomes. The Huntington's Disease Collaborative
11 Research Group. *Cell* 1993; 72: 971-983.
- 12 Havaei M, Davy A, Warde-Farley D, Biard A, Courville A, Bengio Y, *et al.* Brain tumor
13 segmentation with Deep Neural Networks. *Med Image Anal* 2017; 35: 18-31.
- 14 Hering T, Birth N, Taanman JW, and Orth M Selective striatal mtDNA depletion in end-stage
15 Huntington's disease R6/2 mice. *Exp Neurol* 2015; 266: 22-29.
- 16 Hering T, Kojer K, Birth N, Hallitsch J, Taanman JW, and Orth M Mitochondrial cristae
17 remodelling is associated with disrupted OPA1 oligomerisation in the Huntington's disease
18 R6/2 fragment model. *Exp Neurol* 2017; 288: 167-175.
- 19 Herrmann D, and Parlato R C9orf72-associated neurodegeneration in ALS-FTD: breaking
20 new ground in ribosomal RNA and nucleolar dysfunction. *Cell Tissue Res* 2018; 373: 351-
21 360.
- 22 Hilditch-Maguire P, Trettel F, Passani LA, Auerbach A, Persichetti F, and MacDonald ME
23 Huntingtin: an iron-regulated protein essential for normal nuclear and perinuclear organelles.
24 *Hum Mol Genet* 2000; 9: 2789-2797.
- 25 Jesse S, Bayer H, Alupej MC, Zugel M, Mulaw M, Tuorto F, *et al.* Ribosomal transcription is
26 regulated by PGC-1alpha and disturbed in Huntington's disease. *Sci Rep* 2017; 7: 8513.
- 27 Joag H, Ghatpande V, Desai M, Sarkar M, Raina A, Shinde M, *et al.* A role of cellular
28 translation regulation associated with toxic Huntingtin protein. *Cell Mol Life Sci* 2019;

- 1 Kiryk A, Sowodniok K, Kreiner G, Rodriguez-Parkitna J, Sonmez A, Gorkiewicz T, *et al.*
2 Impaired rRNA synthesis triggers homeostatic responses in hippocampal neurons. *Front Cell*
3 *Neurosci* 2013; 7: 207.
- 4 Kreiner G, Bierhoff H, Armentano M, Rodriguez-Parkitna J, Sowodniok K, Naranjo JR, *et al.*
5 A neuroprotective phase precedes striatal degeneration upon nucleolar stress. *Cell Death*
6 *Differ* 2013; 20: 1455-1464.
- 7 Lafontaine DLJ, Riback JA, Bascetin R, and Brangwynne CP The nucleolus as a multiphase
8 liquid condensate. *Nat Rev Mol Cell Biol* 2020;
- 9 Langfelder P, Cattle JP, Chatzopoulou D, Wang N, Gao F, Al-Ramahi I, *et al.* Integrated
10 genomics and proteomics define huntingtin CAG length-dependent networks in mice. *Nat*
11 *Neurosci* 2016; 19: 623-633.
- 12 Latonen L Phase-to-Phase With Nucleoli - Stress Responses, Protein Aggregation and Novel
13 Roles of RNA. *Front Cell Neurosci* 2019; 13: 151.
- 14 Lee J, Hwang YJ, Boo JH, Han D, Kwon OK, Todorova K, *et al.* Dysregulation of upstream
15 binding factor-1 acetylation at K352 is linked to impaired ribosomal DNA transcription in
16 Huntington's disease. *Cell Death Differ* 2011; 18: 1726-1735.
- 17 Lee J, Hwang YJ, Ryu H, Kowall NW, and Ryu H Nucleolar dysfunction in Huntington's
18 disease. *Biochim Biophys Acta* 2014; 1842: 785-790.
- 19 Lee KH, Zhang P, Kim HJ, Mitrea DM, Sarkar M, Freibaum BD, *et al.* C9orf72 Dipeptide
20 Repeats Impair the Assembly, Dynamics, and Function of Membrane-Less Organelles. *Cell*
21 2016; 167: 774-788 e717.
- 22 Levine MS, Klapstein GJ, Koppel A, Gruen E, Cepeda C, Vargas ME, *et al.* Enhanced
23 sensitivity to N-methyl-D-aspartate receptor activation in transgenic and knockin mouse
24 models of Huntington's disease. *J Neurosci Res* 1999; 58: 515-532.
- 25 Lin L, Park JW, Ramachandran S, Zhang Y, Tseng YT, Shen S, *et al.* Transcriptome
26 sequencing reveals aberrant alternative splicing in Huntington's disease. *Hum Mol Genet*
27 2016; 25: 3454-3466.
- 28 Liot G, Valette J, Pepin J, Flament J, and Brouillet E Energy defects in Huntington's disease:
29 Why "in vivo" evidence matters. *Biochem Biophys Res Commun* 2017; 483: 1084-1095.

- 1 Mangiarini L, Sathasivam K, Seller M, Cozens B, Harper A, Hetherington C, *et al.* Exon 1 of
2 the HD gene with an expanded CAG repeat is sufficient to cause a progressive neurological
3 phenotype in transgenic mice. *Cell* 1996; *87*: 493-506.
- 4 McColgan P, Seunarine KK, Razi A, Cole JH, Gregory S, Durr A, *et al.* Selective vulnerability
5 of Rich Club brain regions is an organizational principle of structural connectivity loss in
6 Huntington's disease. *Brain* 2015; *138*: 3327-3344.
- 7 McColgan P, and Tabrizi SJ Huntington's disease: a clinical review. *Eur J Neurol* 2018; *25*:
8 24-34.
- 9 Menalled LB, Kudwa AE, Miller S, Fitzpatrick J, Watson-Johnson J, Keating N, *et al.*
10 Comprehensive behavioral and molecular characterization of a new knock-in mouse model
11 of Huntington's disease: zQ175. *PLoS One* 2012; *7*: e49838.
- 12 Moffitt H, McPhail GD, Woodman B, Hobbs C, and Bates GP Formation of polyglutamine
13 inclusions in a wide range of non-CNS tissues in the HdhQ150 knock-in mouse model of
14 Huntington's disease. *PLoS One* 2009; *4*: e8025.
- 15 Montanaro L, Trere D, and Derenzini M Nucleolus, ribosomes, and cancer. *Am J Pathol*
16 2008; *173*: 301-310.
- 17 Naranjo JR, Zhang H, Villar D, Gonzalez P, Dopazo XM, Moron-Oset J, *et al.* Activating
18 transcription factor 6 derepression mediates neuroprotection in Huntington disease. *J Clin*
19 *Invest* 2016; *126*: 627-638.
- 20 Neureither F, Ziegler K, Pitzer C, Frings S, and Mohrlen F Impaired Motor Coordination and
21 Learning in Mice Lacking Anoctamin 2 Calcium-Gated Chloride Channels. *Cerebellum* 2017;
22 *16*: 929-937.
- 23 Nicolas E, Parisot P, Pinto-Monteiro C, de Walque R, De Vleeschouwer C, and Lafontaine
24 DL Involvement of human ribosomal proteins in nucleolar structure and p53-dependent
25 nucleolar stress. *Nat Commun* 2016; *7*: 11390.
- 26 Nollen EA, Salomons FA, Brunsting JF, van der Want JJ, Sibon OC, and Kampinga HH
27 Dynamic changes in the localization of thermally unfolded nuclear proteins associated with
28 chaperone-dependent protection. *Proc Natl Acad Sci U S A* 2001; *98*: 12038-12043.
- 29 Nunez Villacis L, Wong MS, Ferguson LL, Hein N, George AJ, and Hannan KM New Roles
30 for the Nucleolus in Health and Disease. *Bioessays* 2018; *40*: e1700233.

- 1 Orth M, Bronzova J, Tritsch C, Ray Dorsey E, Ferreira JJ, Gemperli A, *et al.* Comparison of
2 Huntington's Disease in Europe and North America. *Mov Disord Clin Pract* 2017; 4: 358-367.
- 3 Parlato R, and Bierhoff H Role of nucleolar dysfunction in neurodegenerative disorders: a
4 game of genes? . *AIMS Molecular Science* 2015; 2: 211-224
- 5 Parlato R, and Kreiner G Nucleolar activity in neurodegenerative diseases: a missing piece
6 of the puzzle? *J Mol Med (Berl)* 2013; 91: 541-547.
- 7 Parlato R, Rieker C, Turiault M, Tronche F, and Schutz G Survival of DA neurons is
8 independent of CREM upregulation in absence of CREB. *Genesis* 2006; 44: 454-464.
- 9 Penney JB, Jr., Vonsattel JP, MacDonald ME, Gusella JF, and Myers RH CAG repeat
10 number governs the development rate of pathology in Huntington's disease. *Ann Neurol*
11 1997; 41: 689-692.
- 12 Peskett TR, Rau F, O'Driscoll J, Patani R, Lowe AR, and Saibil HR A Liquid to Solid Phase
13 Transition Underlying Pathological Huntingtin Exon1 Aggregation. *Mol Cell* 2018; 70: 588-
14 601 e586.
- 15 Pfister JA, and D'Mello SR Regulation of Neuronal Survival by Nucleophosmin 1 (NPM1) Is
16 Dependent on Its Expression Level, Subcellular Localization, and Oligomerization Status. *J*
17 *Biol Chem* 2016; 291: 20787-20797.
- 18 Potapova TA, Unruh JR, Yu Z, Rancati G, Li H, Stampfer MR, *et al.* Superresolution
19 microscopy reveals linkages between ribosomal DNA on heterologous chromosomes. *J Cell*
20 *Biol* 2019; 218: 2492-2513.
- 21 Rai SN, Singh BK, Rathore AS, Zahra W, Keswani C, Birla H, *et al.* Quality Control in
22 Huntington's Disease: a Therapeutic Target. *Neurotox Res* 2019; 36: 612-626.
- 23 Rekulapally P, and Suresh SN Nucleolus: A Protein Quality Control Compartment. *Trends*
24 *Biochem Sci* 2019; 44: 993-995.
- 25 Riback JA, Zhu L, Ferrolino MC, Tolbert M, Mitrea DM, Sanders DW, *et al.* Composition-
26 dependent thermodynamics of intracellular phase separation. *Nature* 2020; 581: 209-214.
- 27 Rieker C, Engblom D, Kreiner G, Domanskyi A, Schober A, Stotz S, *et al.* Nucleolar
28 disruption in dopaminergic neurons leads to oxidative damage and parkinsonism through
29 repression of mammalian target of rapamycin signaling. *J Neurosci* 2011; 31: 453-460.

- 1 Rodinova M, Krizova J, Stufkova H, Bohuslavova B, Askeland G, Dosoudilova Z, *et al.*
2 Deterioration of mitochondrial bioenergetics and ultrastructure impairment in skeletal muscle
3 of a transgenic minipig model in the early stages of Huntington's disease. *Dis Model Mech*
4 2019; 12
- 5 Saudou F, and Humbert S The Biology of Huntingtin. *Neuron* 2016; 89: 910-926.
- 6 Schindelin J, Arganda-Carreras I, Frise E, Kaynig V, Longair M, Pietzsch T, *et al.* Fiji: an
7 open-source platform for biological-image analysis. *Nat Methods* 2012; 9: 676-682.
- 8 Schludi MH, May S, Grasser FA, Rentzsch K, Kremmer E, Kupper C, *et al.* Distribution of
9 dipeptide repeat proteins in cellular models and C9orf72 mutation cases suggests link to
10 transcriptional silencing. *Acta Neuropathol* 2015; 130: 537-555.
- 11 Sharifi S, and Bierhoff H Regulation of RNA Polymerase I Transcription in Development,
12 Disease, and Aging. *Annu Rev Biochem* 2018; 87: 51-73.
- 13 Shelhamer E, Long J, and Darrell T Fully Convolutional Networks for Semantic
14 Segmentation. *IEEE Trans Pattern Anal Mach Intell* 2017; 39: 640-651.
- 15 Shirasaki DI, Greiner ER, Al-Ramahi I, Gray M, Boontheung P, Geschwind DH, *et al.*
16 Network organization of the huntingtin proteomic interactome in mammalian brain. *Neuron*
17 2012; 75: 41-57.
- 18 Stamatopoulou V, Parisot P, De Vleeschouwer C, and Lafontaine DLJ Use of the iNo score
19 to discriminate normal from altered nucleolar morphology, with applications in basic cell
20 biology and potential in human disease diagnostics. *Nat Protoc* 2018; 13: 2387-2406.
- 21 Stuitje G, van Belzen MJ, Gardiner SL, van Roon-Mom WMC, Boogaard MW, Network
22 R1otEHD, *et al.* Age of onset in Huntington's disease is influenced by CAG repeat variations
23 in other polyglutamine disease-associated genes. *Brain* 2017; 140: e42.
- 24 Tabrizi SJ, Langbehn DR, Leavitt BR, Roos RA, Durr A, Craufurd D, *et al.* Biological and
25 clinical manifestations of Huntington's disease in the longitudinal TRACK-HD study: cross-
26 sectional analysis of baseline data. *Lancet Neurol* 2009; 8: 791-801.
- 27 Tafforeau L, Zorbas C, Langhendries JL, Mullineux ST, Stamatopoulou V, Mullier R, *et al.*
28 The complexity of human ribosome biogenesis revealed by systematic nucleolar screening of
29 Pre-rRNA processing factors. *Mol Cell* 2013; 51: 539-551.

- 1 Taslimi A, Vrana JD, Chen D, Borinskaya S, Mayer BJ, Kennedy MJ, *et al.* An optimized
2 optogenetic clustering tool for probing protein interaction and function. *Nat Commun* 2014; 5:
3 4925.
- 4 Tauber E, Miller-Fleming L, Mason RP, Kwan W, Clapp J, Butler NJ, *et al.* Functional gene
5 expression profiling in yeast implicates translational dysfunction in mutant huntingtin toxicity.
6 *J Biol Chem* 2011; 286: 410-419.
- 7 Tiku V, Kew C, Mehrotra P, Ganesan R, Robinson N, and Antebi A Nucleolar fibrillarin is an
8 evolutionarily conserved regulator of bacterial pathogen resistance. *Nat Commun* 2018; 9:
9 3607.
- 10 Trettel F, Rigamonti D, Hilditch-Maguire P, Wheeler VC, Sharp AH, Persichetti F, *et al.*
11 Dominant phenotypes produced by the HD mutation in STHdh(Q111) striatal cells. *Hum Mol*
12 *Genet* 2000; 9: 2799-2809.
- 13 Tsoi H, and Chan HY Expression of expanded CAG transcripts triggers nucleolar stress in
14 Huntington's disease. *Cerebellum* 2013; 12: 310-312.
- 15 Tsoi H, Lau TC, Tsang SY, Lau KF, and Chan HY CAG expansion induces nucleolar stress
16 in polyglutamine diseases. *Proc Natl Acad Sci U S A* 2012; 109: 13428-13433.
- 17 Vashishta A, Slomnicki LP, Pietrzak M, Smith SC, Kolikonda M, Naik SP, *et al.* RNA
18 Polymerase 1 Is Transiently Regulated by Seizures and Plays a Role in a Pharmacological
19 Kindling Model of Epilepsy. *Mol Neurobiol* 2018; 55: 8374-8387.
- 20 Wang HF, Takenaka K, Nakanishi A, and Miki Y BRCA2 and nucleophosmin coregulate
21 centrosome amplification and form a complex with the Rho effector kinase ROCK2. *Cancer*
22 *Res* 2011; 71: 68-77.
- 23 Xie Y, Hayden MR, and Xu B BDNF overexpression in the forebrain rescues Huntington's
24 disease phenotypes in YAC128 mice. *J Neurosci* 2010; 30: 14708-14718.
- 25 Yao RW, Xu G, Wang Y, Shan L, Luan PF, Wang Y, *et al.* Nascent Pre-rRNA Sorting via
26 Phase Separation Drives the Assembly of Dense Fibrillar Components in the Human
27 Nucleolus. *Mol Cell* 2019;
- 28 Zhu L, Richardson TM, Wacheul L, Wei MT, Feric M, Whitney G, *et al.* Controlling the
29 material properties and rRNA processing function of the nucleolus using light. *Proc Natl Acad*
30 *Sci U S A* 2019; 116: 17330-17335.

1 Zuccato C, Ciammola A, Rigamonti D, Leavitt BR, Goffredo D, Conti L, *et al.* Loss of
2 huntingtin-mediated BDNF gene transcription in Huntington's disease. *Science* 2001; 293:
3 493-498.
4
5

1 **Figure Legends**

2 **Figure 1: Cells expressing Huntingtin mutations display altered distribution of**
3 **nucleolar NPM1 and alterations of pre-rRNA processing.** (A) Representative confocal
4 images of NPM1 and NCL immunofluorescence staining in Q7/7 and Q111/111 cells. (B)
5 Quantification of the percentage of nuclei with nucleolar ring-like NCL and NPM1 signals.
6 The percentage of nuclei with nucleolar NPM1 is significantly reduced in the Q111/111 cells
7 by Mann-Whitney U test ($p=0.014$) (n : number of nuclei = 421 in Q7/7 and 634 in Q111/111;
8 N : fields of view in two independent experiments = 6 for Q7/7 and Q111/111). Values
9 represent mean values. Error bars represent SEM. * $p<0.05$. Detailed statistical information
10 is included in the Supplementary Statistical Information file. (C) Mouse pre-rRNA processing
11 pathway. Three out of four mature rRNAs (the 18S, 5.8S, and 28S) are encoded in a single
12 polycistronic transcript synthesized by RNA polymerase I, the 47S. Mature rRNAs are
13 embedded in 5' and 3' external transcribe spacers (5'- and 3'-ETS) and internal transcribed
14 spacers 1 and 2 (ITS1 and 2) and are produced by extensive processing of the 47S.
15 Processing sites (A', A0, 1 etc.) are indicated in blue. There are two alternative processing
16 pathways in mouse (pathways 1 and 2, boxed) according to initial processing in 5'-ETS or
17 ITS1, respectively. (D) Total RNA was extracted, separated on denaturing high-resolution
18 agarose gel, stained with ethidium bromide to reveal large mature rRNAs, or processed for
19 Northern blotting. Species labeled '1 to 4' (in red) are extended forms of the 34S pre-rRNAs
20 that were not previously described. Species '2, 3, and 4' are detected in the control cells
21 (Q7/7). Species '1' is only detected in the mutant cells (Q111/Q111). Species '1' is formed at
22 the cost of species '2' (the upper band of the doublet). The boxed area highlights the
23 appearance of species '1' in Q111/Q111 cells, which is concomitant with the disappearance
24 of species '2'. (E) The samples described in panel (D) were run in a longer migration to
25 separate more efficiently the doublet corresponding to bands '2 and 3'. (F) Ethidium bromide
26 staining revealing that the steady state levels of 18S and 28S rRNA are not grossly affected.
27

1 **Figure 2: De-localization of NPM1 and NCL and altered nuclear distribution of mHTT**
2 **inclusions upon irreversible induction of nucleolar stress in striatal neurons. (A)**
3 Representative confocal images of striatal sections from control, TIF-IA^{D1Cre}, R6/2 and R6/2;
4 TIF-IA^{D1Cre} double mutant (dm) mice at 9 weeks co-immunostained with antibodies against
5 the nucleolar marker NPM1 and NCL, and p62 and mHTT (EM48), respectively. Insets are
6 high magnification of the nuclei highlighted by the white arrow. Scale bar: 20 μ m, 10 μ m
7 (insets). (B) mHTT nuclear distribution measured as the ratio between mHTT mean intensity
8 in the nucleoplasm and in the nuclear inclusions in R6/2 (N=4) and dm (N=4) mice. mHTT
9 intensity in the nucleoplasm of dm is significantly lower in comparison to R6/2 mice (Mann-
10 Whitney U test, $p = 0.03$). (C) Higher nucleolar integrity assessed by NCL intensity in the
11 nucleus correlates with a higher nucleoplasm/inclusion mHTT intensity ratio in R6/2 (n:
12 number of nuclei=335, N: number of mice=4) and dm mice (n: number of nuclei=296, N:
13 number of mice=4); ($p < 0.0001$ for R6/2 and dm; Pearson coefficient r for R6/2 is 0.67 and for
14 the dm 0.68). (D) Diagram showing endurance (in s) on an accelerating rotarod in the four
15 experimental groups at different ages (9, 10 and 11 weeks, w). Significant variation between
16 genotypes by two-way ANOVA ($p < 0.0001$); significant differences between groups for each
17 age were determined by Tukey's multiple comparison: R6/2 vs. dm: $p = 0.012$ at 10 weeks,
18 $p = 0.003$ at 11 weeks. N: number of mice, control: 8, TIF-IA^{D1RCre}: 6, R6: 12, dm: 12. (E)
19 Diagram showing the results of grip strength test in the four experimental groups at different
20 ages (9, 10 and 11 weeks, w). Significant variation in age and genotype by two-way ANOVA
21 ($p < 0.0006$); significant differences between groups for each age were determined by
22 Tukey's multiple comparison. N control: 8, TIF-IA^{D1RCre}: 6, R6: 12, dm: 12. Legend: * $p < 0.05$,
23 ** $p < 0.01$, *** $p < 0.001$. Detailed statistical information is included in the Supplementary
24 Statistical Information file.

25
26 **Figure 3: mHTT nuclear distribution changes at different stages in the striatum of**
27 **zQ175 knock-in model. (A) Relative expression of *D2r* and *D1r* mRNA in the striatum by**
28 qRT-PCR at 3, 4, 5, 6 and 10 months (mo) in control (N=6, 8, 7, 10, 5) and zQ175 mutant

1 (N=6, 8, 6, 8, 5) mice is expressed as fold change to respective controls. Significantly
2 decreased relative expression of *D2r* at 5 (p= 0.014), 6 (p=0.012), 10 months (p=0.032) and
3 of *D1r* at 10 months (p=0.032) by Mann-Whitney U test. (B, C) Representative confocal
4 images of striatal sections from zQ175 mice at 5 and 10 months stained with antibodies
5 against mHTT (EM48) and counterstained with DAPI to visualize the nuclei, and with
6 antibodies against mHTT (EM48) and NCL. Scale bar: 20 μ m (B), 10 μ m (C). (D)
7 Quantification of the nuclei with mHTT inclusion bodies in the zQ175 mice at 5 and 10
8 months shows a significant increase at 10 months by Mann-Whitney U test (p=0.008). (E)
9 Non-significant statistical differences in the mean area of the mHTT inclusion signal by
10 Mann-Whitney U test (p=0.09) between zQ175 mice at 5 and 10 months. (F) Nuclear
11 distribution of mHTT is measured as the ratio between mHTT mean intensity in the
12 nucleoplasm and in the nuclear inclusions at 5 and 10 months. mHTT intensity in the
13 nucleoplasm at 10 months is significantly lower by Mann-Whitney U test (p=0.016). N:
14 number of mice = 5; values represent mean values. Error bars represent SEM. * p<0.05, **
15 p<0.01.

16

17 **Figure 4: rDNA transcription is unaffected in striata of zQ175 mice at both pre- and**
18 **early manifest stages.** (A) Schematic representation of the 47S pre-rRNA transcript
19 including the position of the primers used for qRT-PCR and of the riboprobe used for RNA
20 ISH within the 5'-external transcribed spacer (5'-ETS). (B-D) Analysis of 47S pre-rRNA and
21 mature 18S rRNA relative expression in the striatum by qRT-PCR at 5 and 10 months in
22 controls (N= 6-8) and zQ175 (N= 4-6) shows no significant differences by Mann-Whitney U
23 test. (E) Representative RNA ISH images of 5 and 10 month-old control and zQ175 mice
24 showing the 47S pre-rRNA signals as blue punctuate signals within the nuclei in striatal
25 sections. Scale bar: 20 μ m. (F) No significant difference in the average number of 47S pre-
26 rRNA foci per striatal cell at 5 and 10 months in control (N= 9,7) and zQ175 mice (N= 7,6) by
27 Mann-Whitney U test (p=0.09 at 5 months). (G) Representative Northern blots for the

1 analysis of 5.8S rRNA in striata from controls (N= 10) and zQ175 (N= 8) at 5 months and
2 densitometric analysis normalized by 5S rRNA. Error bars represent SEM.

3

4 **Figure 5: Redistribution of NPM1 in the striatum of pre-symptomatic zQ175 mice.** (A,B)

5 Representative confocal images of striatal sections stained for NPM1 (green) and NCL (red)

6 in control and zQ175 mice at 5 and 10 months. Scale bar: 20 μ m. (C) Quantification of the

7 percentage of nuclei with nucleolar localization of NCL or NPM1 expressed as percentage of

8 nuclei showing them as a circular nucleolar signal at 5 and 10 months in control and zQ175

9 mice (N: number of mice, control: 7,7,5,3 and zQ175: 8,5,5,5). Significant decrease in the

10 number of nuclei showing nucleolar NPM1 in the zQ175 mice at 5 months in comparison to

11 their respective controls by Mann-Whitney U test ($p= 0.02$). Values represent mean. Error

12 bars represent SEM. * $p<0.05$. (D) Super-resolution (STED) microscopic images showing

13 loss of NPM1 (red) ring-like organization and its association with disperse mHTT (green)

14 signals at 5 months, but not at 10 months. (E) Line scans through the boxed regions

15 containing the nucleolus and mHTT inclusion describe the distribution of NPM1 and mHTT

16 signals in the zQ175 mice at both ages. A close proximity of mHTT and NPM1 signals at 5

17 months can be observed. Scale bar: 2 μ m, zoom: 100 nm.

18

19 **Figure 6: NPM1 nucleolar localization is altered in the skeletal muscle (quadriceps) of**

20 **zQ175 mice at a symptomatic stage and downregulated rDNA transcription at an early**

21 **manifest stage.** (A) Representative confocal images of quadriceps cryosections stained for

22 NPM1 (green) or NCL (red) in control and zQ175 mice at 5 and 10 months. Nuclei are

23 labeled with DAPI (blue). The arrows point out to NPM1 or NCL signal. Scale bar: 20 μ m. (B)

24 Quantification of the percentage of nuclei with nucleolar localisation of NPM1 or NCL at 5

25 and 10 months (mo) in control (N, number of mice, NPM: 4, 4; NCL: 3, 4) and zQ175 (N:

26 number of mice, NPM: 5, 5; NCL: 3, 6) mice shows no significant differences. (C)

27 Quantification of the mean area of the NPM1 or NCL signal (in μ m²) per DAPI positive nuclei

28 at 5 and 10 months (mo) in control (N for NPM1: 5, 4; for NCL: 3, 4) and zQ175 (N for NPM1:

1 4, 6; for NCL: 3, 5) mice shows a significant reduction in nucleolar NPM1 signal at 10 months
2 by Mann-Whitney U test ($p=0.038$). * $p<0.05$. (D) Analysis of 47S pre-rRNA and mature 18S
3 rRNA levels by qRT-PCR at 5 and 10 months in the skeletal muscle of controls ($N=3-4$) and
4 zQ175 ($N=5-7$) expressed as fold change to respective controls. 47S pre-rRNA is
5 significantly reduced using primer pair 47S2 on the zQ175 mice at 10 months by Mann-
6 Whitney U test ($p=0.012$). Values represent mean. Error bars represent SEM. * $p<0.05$.

7

8 **Figure 7: NPM1 signal is reduced in muscle (quadriceps) biopsies of early-**
9 **Huntington's disease patients.** (A) Representative confocal images of human skeletal
10 muscle (quadriceps) cryosections immunostained for NPM1 (green) or NCL (red) in
11 Huntington's disease patients at different stages and in age-matched controls. Nuclei are
12 labelled with DAPI (blue). The arrows point to NPM1 or NCL signals. Scale bar: $20\mu\text{m}$. (B)
13 Quantification of the percentage of nuclei showing nucleolar NPM1 signal in Huntington's
14 disease patients in comparison with age-matched controls ($N=5$ for each group), and
15 indicating significant decreased NPM1 in early Huntington's disease (early-HD) by Kruskal-
16 Wallis test and Dunn's multiple comparison ($p=0.003$ early-HD vs. controls). No significant
17 differences in the percentage of nuclei with nucleolar NCL. (C) Mean area of the NPM1
18 signal (in μm^2) per DAPI positive nuclei in control, pre- and early-Huntington's disease
19 individuals ($N=5$ for each group). Statistically significant decrease of NPM1 signal area in
20 early Huntington's disease compared to controls by Kruskal-Wallis test and Dunn's multiple
21 comparison ($p=0.01$). No significant differences in the mean area of the NCL signal (in μm^2)
22 between the different groups. Error bars represent SEM. * $p<0.05$, ** $p<0.01$; detailed
23 statistical information is included in the Supplementary Statistical Information file.

24

25

26

27

28

1 **Acknowledgements**

2 We thank all human participants for their participation and donation of tissue samples, and
3 CHDI for providing the zQ175 mice. We also thank Dr. Gillian Bates for providing the S829
4 antibody, Dr. Jose Naranjo for providing the StHdh cells and protocols, Dr. Xunlei Zhou for
5 her initial help with cell cultures. Barbara Kurpiers for her assistance with the behavioral
6 tests, Dr. Nina Ullrich for assistance with the Sunset assay, and Dr. Rosario Piro for
7 assistance with statistical analysis.

8

9 **Conflict of interest statement**

10 The authors report no competing interests.

11

12 **Author contribution**

13 AS, RM, STS, LW, FT, DP, CL, KK, JK, TH, CP, RP: performed experiments; AS, MO, RM,
14 STS, FT, DP, CL, JK, CP, AN, GK, JK, DLJ, BL, RP: analyzed data; AS, MO, AN, JK, DLJ,
15 BL, RP: supervised experimental work; AN, GK: contributed antibodies and mouse lines;
16 MO: contributed human muscle biopsies and study design; MO, RP: conceived the study;
17 AS, MO, DLJ, BL, RP: wrote the manuscript. The first draft of the manuscript was written by
18 RP and all authors commented on previous versions of the manuscript. All authors read and
19 approved the final manuscript.

20

21 **Statement regarding the ethical use of human material and animals**

22 The ethics committee at Ulm University approved the study (Protocol number: 165/12), and
23 written informed consent was obtained from each participant.

24 Procedures involving animal care and use were approved by the Committee on Animal Care
25 and Use (Regierungspräsidium Karlsruhe, Germany, Animal Ethic Protocols: 34-9185.81/G-
26 297/14 and 35-9185.81/G-102/16) in accordance with the local Animal Welfare Act and the
27 European Communities Council Directives (2012/707/EU).

1 **Funding**

2 This work was funded by the “Deutsche Forschungsgemeinschaft” DFG project PA 1529/2-1
3 and by the European Huntington’s Disease Network seed fund project 753 to RP, by the
4 CHDI Foundation Inc. (A-7324 to MO), by the Graduate School CEMMA (GRK1789) to BL,
5 by the German Academic Exchange Service (DAAD) project number: 91609354, section
6 ST24 and the Academic Funding 2016 Sapienza RP116155037D13E1 to DP. Research in
7 the Lab of D.L./J.L. is supported by the Belgian Fonds de la Recherche Scientifique
8 (F.R.S./FNRS), the Université Libre de Bruxelles (ULB), the Région Wallonne (DGO6) [grant
9 RIBO*cancer* n°1810070], the Fonds Jean Brachet, and the International Brachet Stiftung.

10

11 **Data availability**

12 The raw data that support the findings of this study are available under “Supplementary
13 statistical information” and from the corresponding author upon reasonable request.

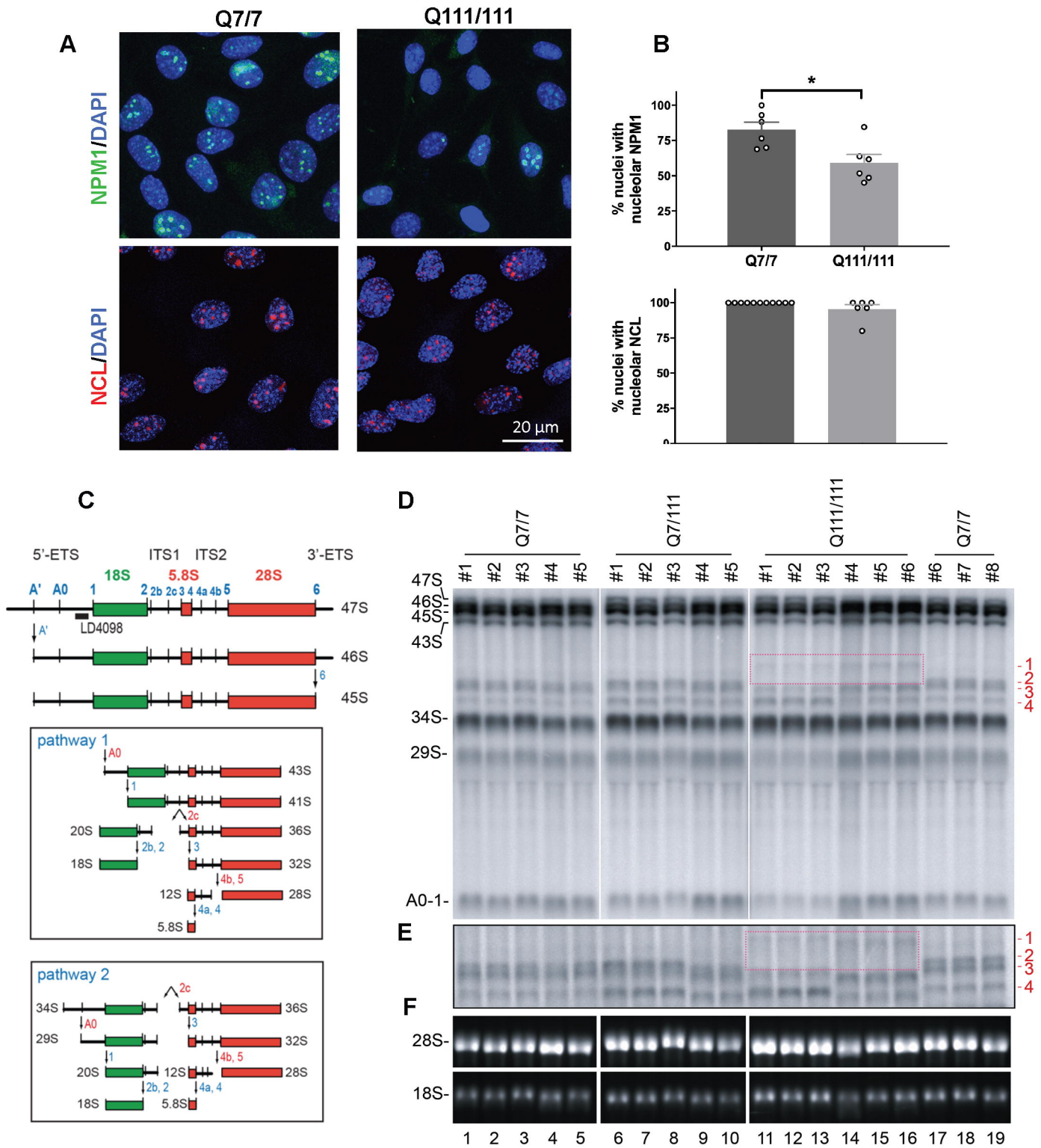


Figure 1

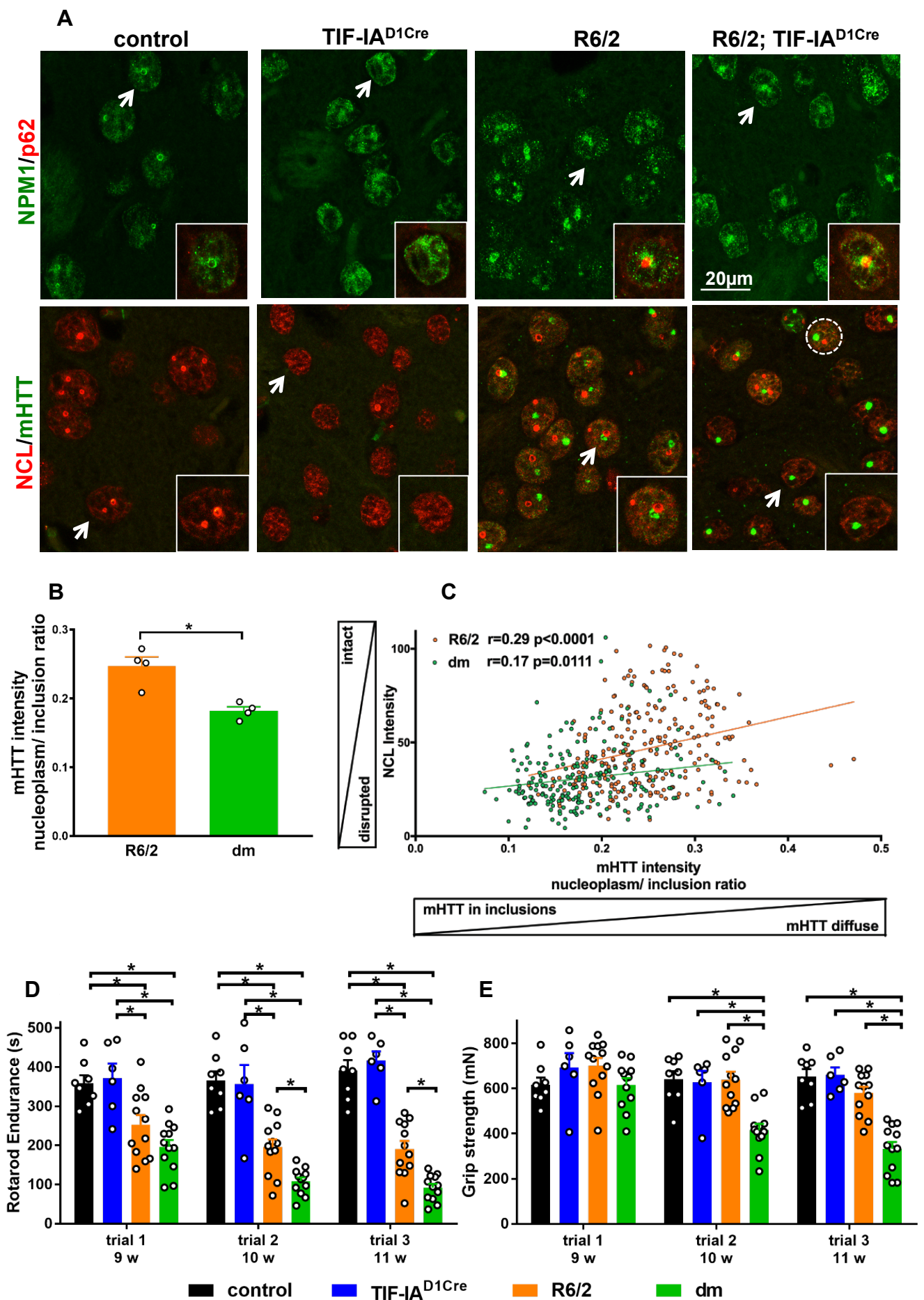


Figure 2

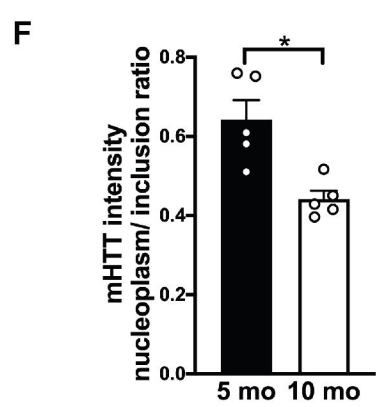
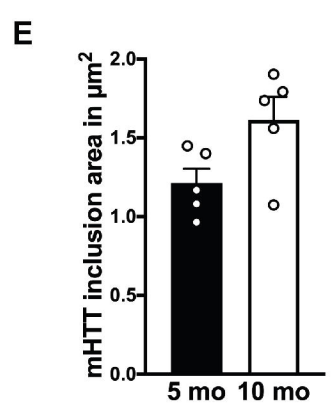
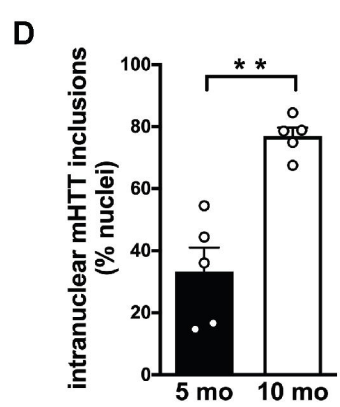
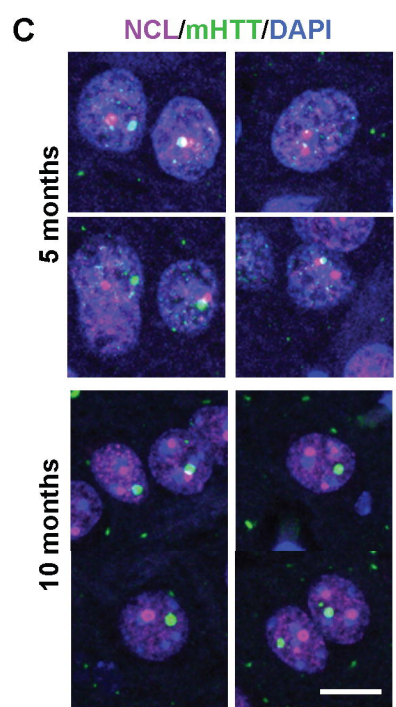
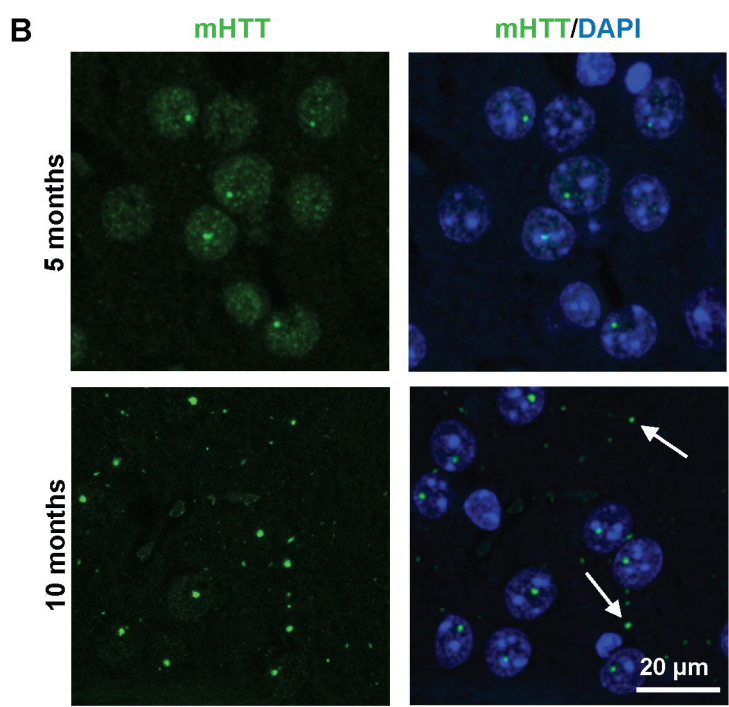
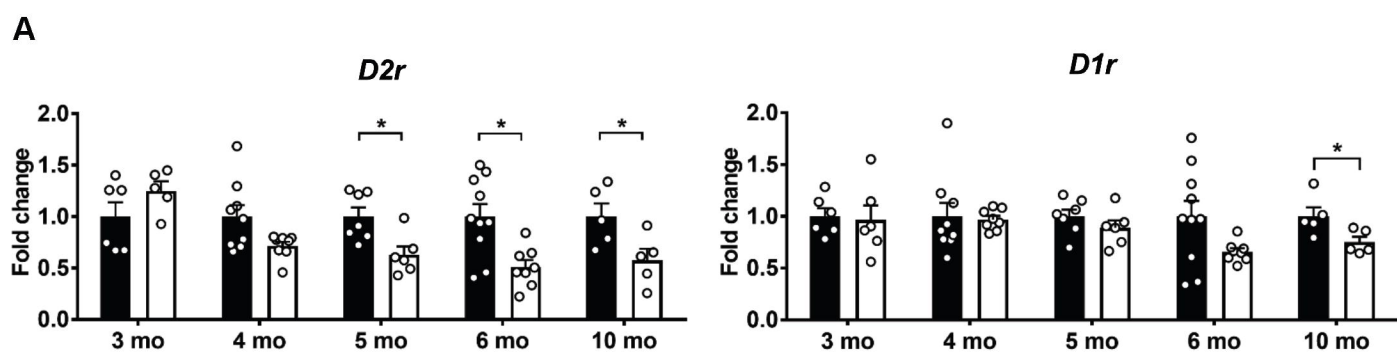


Figure 3

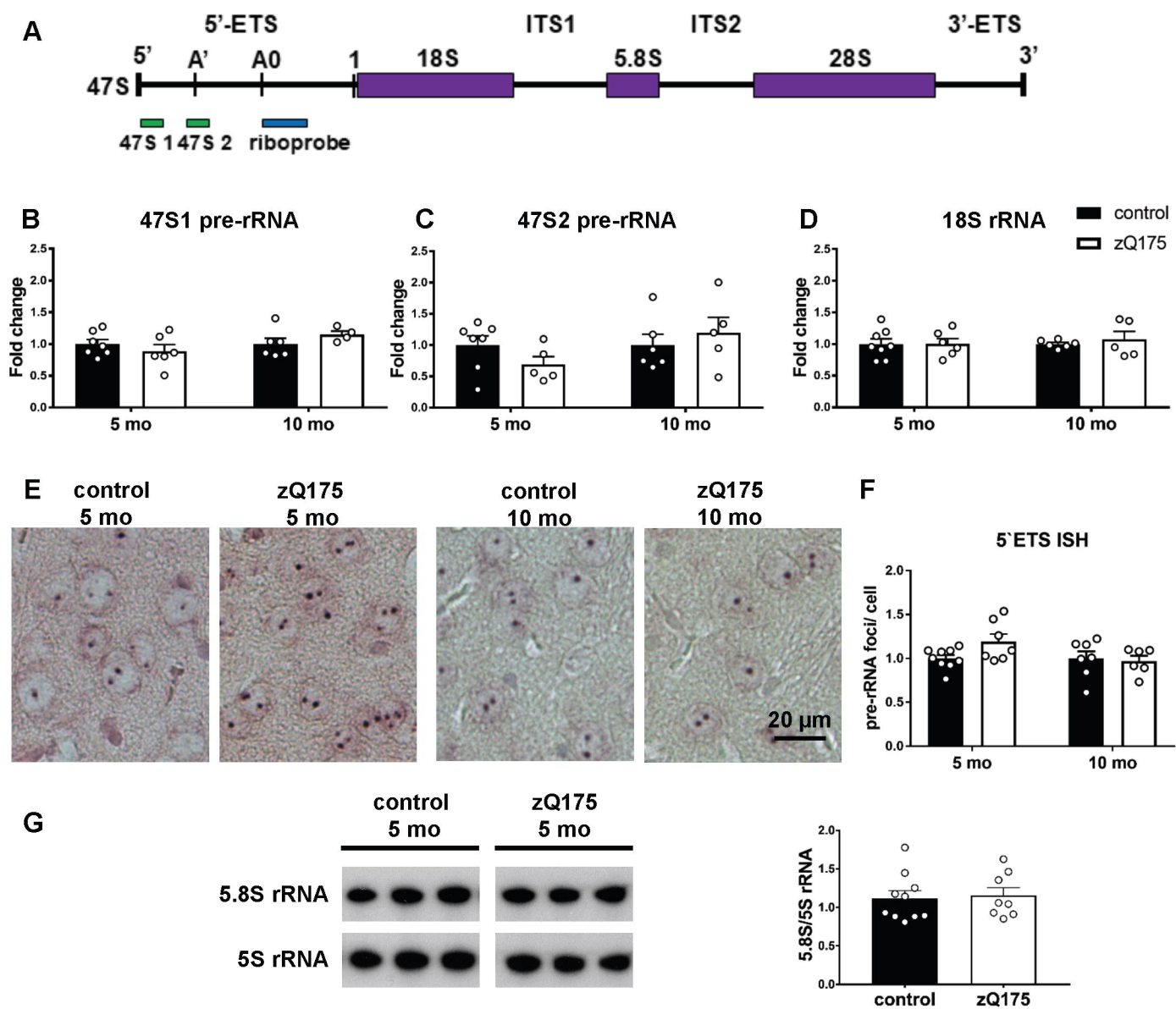


Figure 4

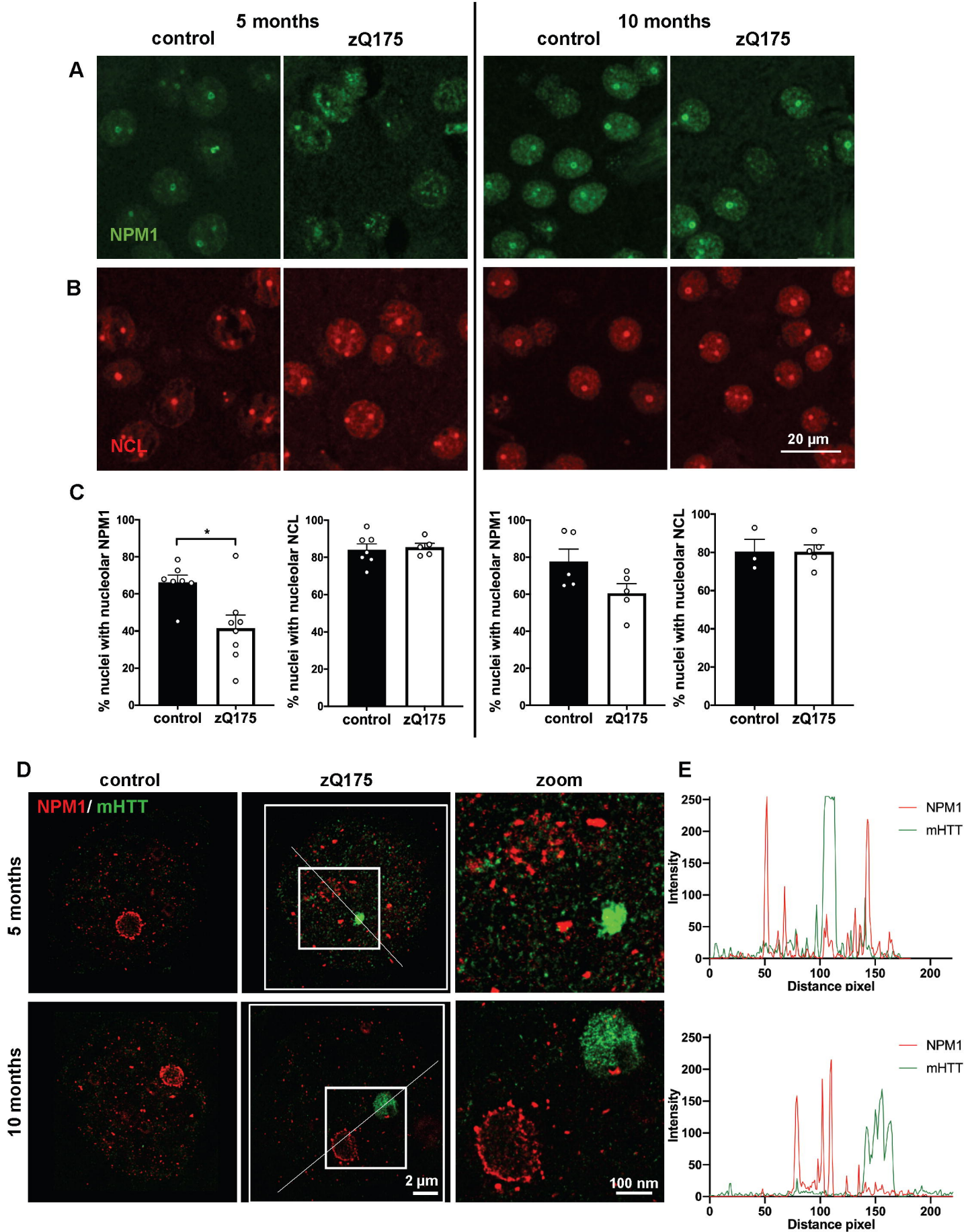
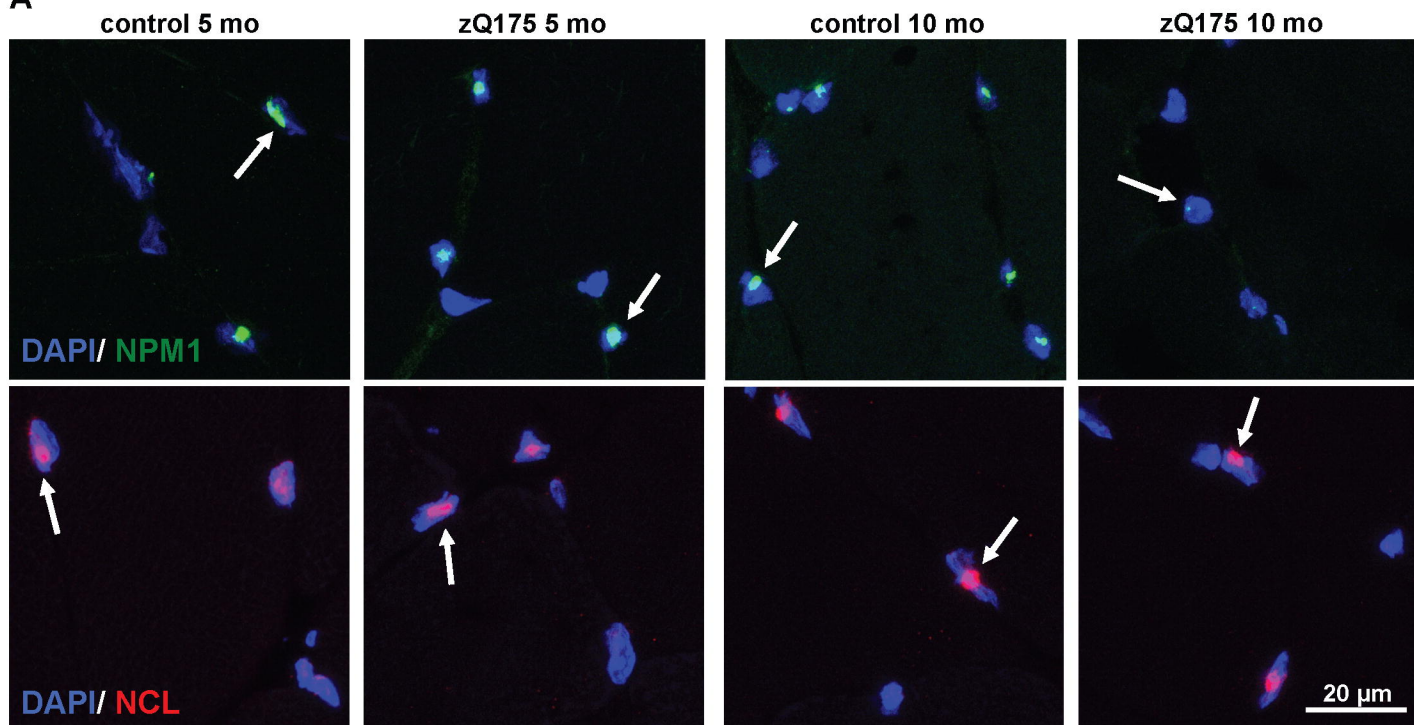


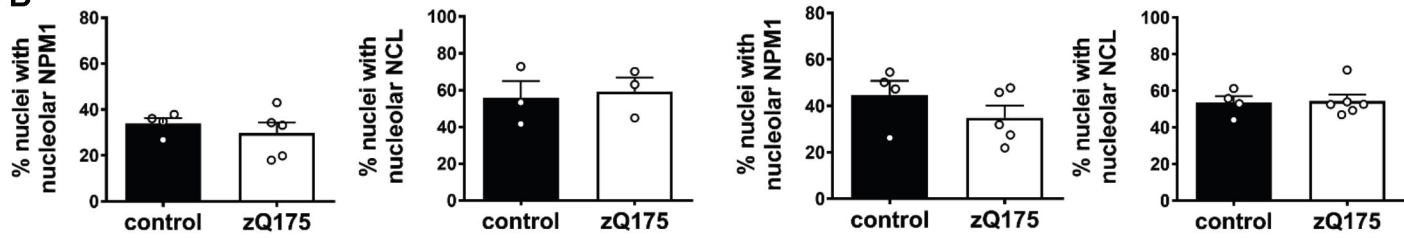
Figure 5

quadriceps

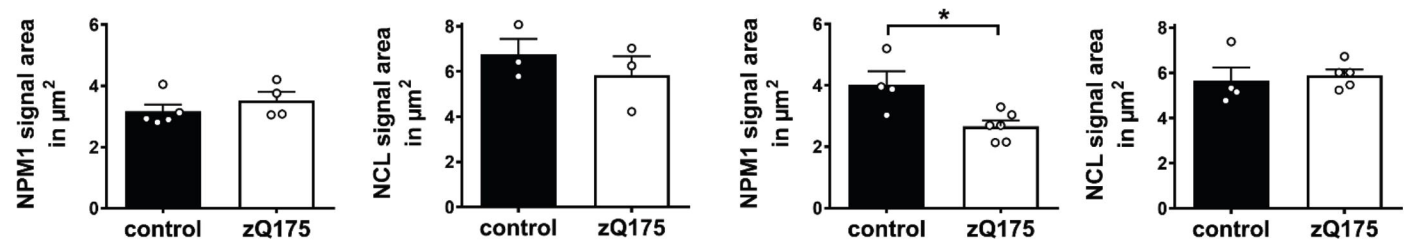
A



B



C



D

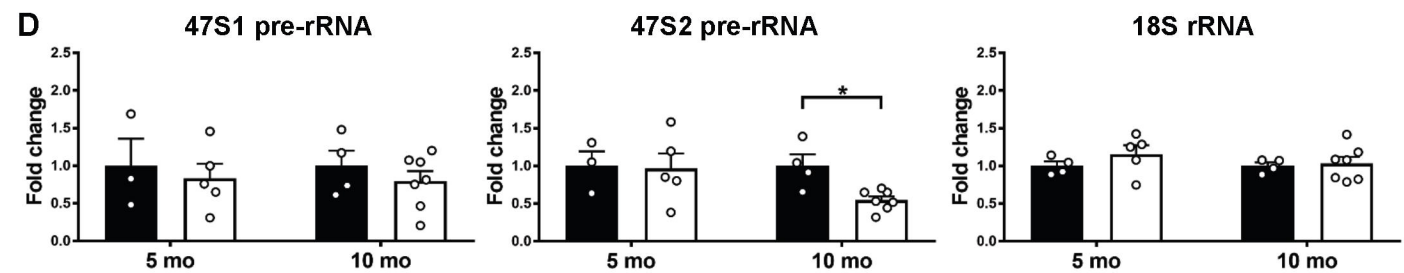


Figure 6

quadriceps

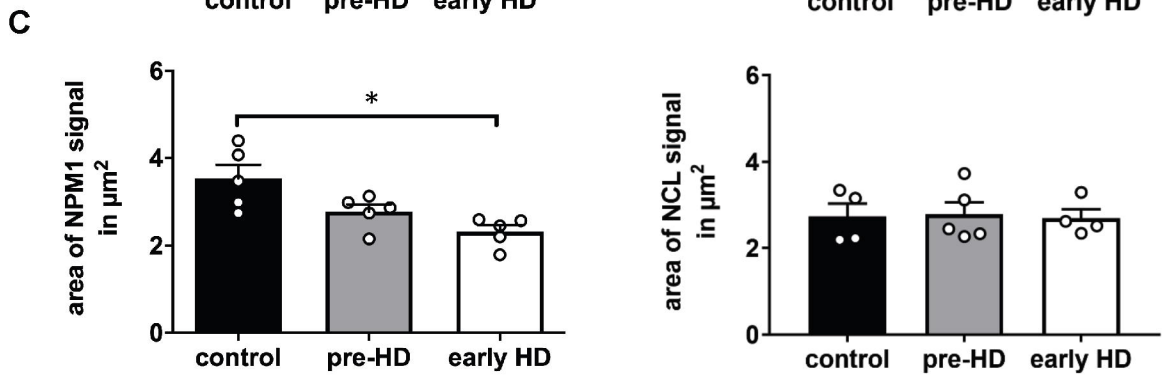
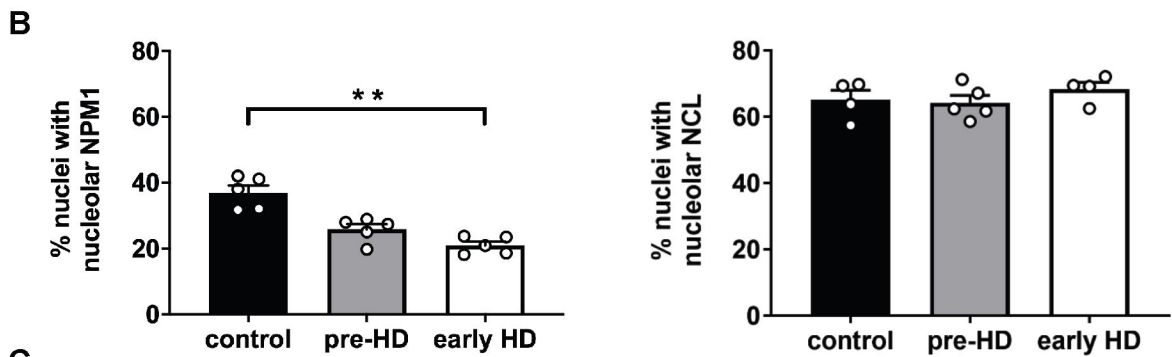
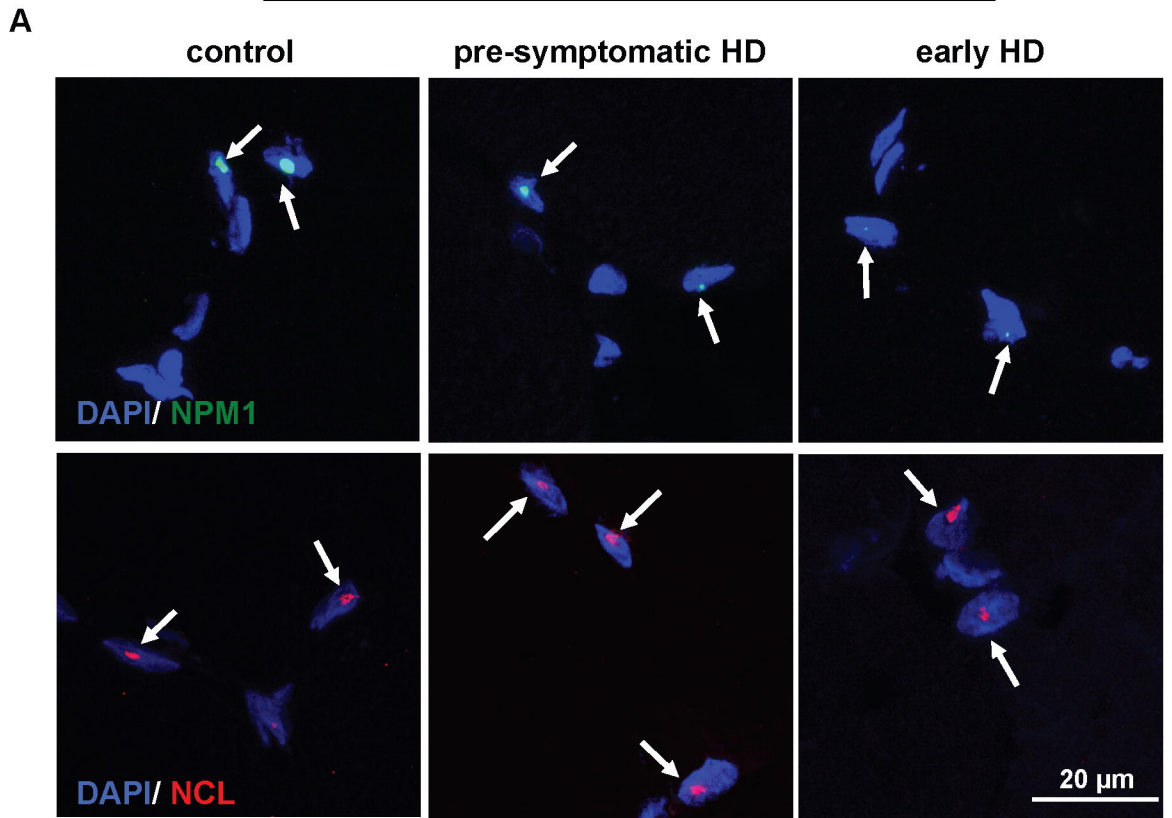


Figure 7